J. Fluid Mech. (2019), *vol.* 875, *pp.* 254–285. © Cambridge University Press 2019
doi:10.1017/jfm.2019.467

Sound and turbulence modulation by particles in high-speed shear flows

David A. Buchta[1],†, **Gregory Shallcross**[2] **and Jesse Capecelatro**[2]

[1]Coordinated Science Laboratory, University of Illinois at Urbana–Champaign, Urbana, IL 61801, USA
[2]Department of Mechanical Engineering, University of Michigan, Ann Arbor, MI 48109, USA

(Received 10 November 2018; revised 6 June 2019; accepted 6 June 2019;
first published online 18 July 2019)

High-speed free-shear-flow turbulence, laden with droplets or particles, can radiate weaker pressure fluctuations than its unladen counterpart. In this study, Eulerian–Lagrangian simulations of high-speed temporally evolving shear layers laden with monodisperse, adiabatic, inertial particles are used to examine particle–turbulence interactions and their effect on radiated pressure fluctuations. An evolution equation for gas-phase pressure intensity is formulated for particle-laden flows, and local mechanisms of pressure changes are quantified over a range of Mach numbers and particle mass loadings. Particle–turbulence interactions alter the local pressure intensity directly via volume displacement (due to the flow of finite-size particles) and drag coupling (due to local slip velocity between phases), and indirectly through significant turbulence changes. The sound radiation intensity near subsonic mixing layers increases with mass loading, consistent with existing low Mach number theory. For supersonic flows, sound levels decrease with mass loading, consistent with trends observed in previous experiments. Particle-laden cases exhibit reduced turbulent kinetic energy compared to single-phase flow, providing one source of their sound changes; however, the subsonic flow does not support such an obvious source-to-sound decomposition to explain its sound intensity increase. Despite its decrease in turbulence intensity, the louder particle-laden subsonic flows show an increase in the magnitude and time-rate-of-change of fluid dilatation, providing a mechanism for its increased sound radiation. Contrasting this, the quieter supersonic particle-laden flows exhibit decreased gas-phase dilatation yet its time-rate-of-change is relatively insensitive to mass loading, supporting such a connection.

Key words: aeroacoustics, compressible turbulence, particle/fluid flow

1. Introduction

Pressure fluctuations from high-speed flows pose serious risks and design challenges in many engineering applications. For example, there is a need to reduce the sound intensity near aircraft during take-off and landing to protect personnel (Kaltenbach, Maschke & Klinke 2008). In addition, regulations are placed to reduce environmental noise pollution from commercial aircraft near cities, described in Bowes *et al.* (2009). Launch pad configurations for rockets address some of these issues by using water

---

† Email address for correspondence: buchta1@illinois.edu

injection systems to reduce pressure fluctuations and thermal loading (Himelblau *et al.* 2001; Ignatius, Sathiyavageeswaran & Chakravarthy 2014). In such configurations, sound reduction depends on the injection geometry, injection flow rate and mass flux ratio (Zoppellari & Juve 1997; Krothapalli *et al.* 2003; Norum 2004), in addition to jet temperature (Norum 2004; Henderson 2010). Microjet injection of water into high-speed jet turbulence has been observed to reduce far-field sound levels by 2–6 dB using 5 %–17 % of the mass of the gas jet (Krothapalli *et al.* 2003). At even larger mass loadings (>100 % of jet mass), a 12 dB reduction of the sound near rocket engine exhausts was achieved (Zoppellari & Juve 1997). However, in similar jet configurations, sound radiation has been observed to increase due to fluid injection, suggesting its control and mechanisms toward noise reduction are not universal (e.g. Gilinsky, Bhat & Seiner 1994, and references therein).

Velocity fluctuations in high-speed shear-flow turbulence provide sources of radiated pressure fluctuations (Lighthill 1952). For supersonic jets injected with water azimuthally near the jet exit, particle image velocimetry (PIV) data show a reduction in turbulence intensity without a sizable change to the mean flow profile (Krothapalli *et al.* 2003), which has implications for the radiated sound. Turbulence correlation length scales also decrease from water droplet-injected shear layers (Krothapalli *et al.* 2003). In addition, micro-jet injection leads to a streamwise oriented vorticity pattern. Without fluid injection, similar vorticity structures have been observed through geometric modifications to the jet nozzles. By adding chevrons (Alkislar & Butler 2007) or likewise using contoured nozzle inserts (e.g. Murray & Lyons 2016), aimed to augment near-nozzle shear layer development, these strategies also achieve a sound reduction, which suggests a shared reduction mechanism with water injection via changes to the turbulence. In isolation, the sensitivity of sound radiation to reduced turbulence correlation, intensity and relative convection velocity are known to a degree (Lighthill 1952; Ffowcs Williams 1963). However, the mechanisms of how a disperse phase (e.g. droplets or particles) couple to the turbulence and pressure field are not fully understood, which limits advancements toward controlling such flows.

Since inertial particles are known to modify incompressible turbulence (see e.g. Balachandar & Eaton 2010, and references therein), these effects, when translated into a compressible regime, are expected to change the pressure fluctuations and sound field radiation. Drag induced by individual particles in turbulent flows can enhance or suppress velocity-fluctuation amplitudes over a wide range of scales, which depend on, for example, the particle size relative to the Kolmogorov length scale, the mean velocity difference between the phases and the particle-to-fluid mass ratio (Elghobashi & Truesdell 1993; Balachandar & Eaton 2010; Capecelatro, Desjardins & Fox 2015, 2018). In the dilute limit, gas-phase turbulence accumulates particles in high-strain regions of the flow (Eaton & Fessler 1994; Rouson & Eaton 2001; Marchioli & Soldati 2002; Balachandar & Eaton 2010), and at higher particle loading it can give rise to the spontaneous generation of densely packed particle regions (Glasser, Sundaresan & Kevrekidis 1998; Noymer & Glicksman 2000; Agrawal *et al.* 2001; Capecelatro *et al.* 2015), i.e. clusters, which have been observed to hinder mixing between the phases (Agrawal *et al.* 2013; Shaffer *et al.* 2013) and amplify the aforementioned two-way-coupled effects. Recent data show that large-scale velocity gradients affect the turbulent transport of small (Kolmogorov-scale) heavy particles and the clustering process at small scales (Nicolai, Jacob & Piva 2013). Gualtieri, Picano & Casciola (2009) demonstrated that large-scale shear generates anisotropic velocity fluctuations which, in turn, arrange particle configurations in directionally biased clusters. In temporally developing shear layers, the mixing layer growth rate and turbulent kinetic energy (TKE) were observed to reduce with mass loading; however, these changes were insensitive to the Stokes numbers considered (Miller & Bellan 1999; Okong'o & Bellan 2004; Leboissetier, Okong'o & Bellan 2005). Similarly, for homogeneous shear turbulence, Battista *et al.* (2018) recently demonstrated that particles with Stokes number $St_\eta = O(1)$, based on the Kolmogorov scale, suppress TKE across the entire range of resolved scales as the mass loading is increased.

Using the foundational aeroacoustics theory of Lighthill (1952), Crighton & Ffowcs Williams (1969) showed that a disperse phase (such as air bubbles or dust particles) flowing in turbulence has additional sources of sound via volume fraction and interphase force mechanisms. Atop the sound from the turbulence, these additional sound sources are anticipated to be substantial, with an up to 20 dB increase in sound pressure levels (Crighton & Ffowcs Williams 1969). Contrary to these theoretical estimates, micro-droplet water injection into the high-speed-jet shear layers reduce sound intensity (Krothapalli *et al.* 2003), suggesting, in part, unknown sound reduction mechanisms. This contradiction has consequence and begs the question: are observed sound reductions near high-speed jets, injected with water droplets, formed from a mixture of sound reduction mechanisms that outpace theoretically large sound sources from the disperse phase itself? The answer has implications for sound-reduction strategies applied to single-phase turbulence, which inherently lack potentially loud sound sources due to particles. As will be shown, results indicate an important Mach number and mass loading dependence for sound and turbulence changes, which suggests extensions to theoretical expectations for regimes considered here. These concepts will be revisited in § 4.

Eulerian–Lagrangian simulations of particle-laden free-shear-flow turbulence are used to provide the space–time dynamics leading to changes in the near-field pressure fluctuations compared to unladen turbulence. In the following section, starting from a mesoscale description for compressible two-phase flows, a transport equation for the gas-phase pressure intensity in the presence of particles is derived. The free-shear-flow turbulence configurations and numerical methods are discussed in § 3. Analysis of turbulence statistics for the parametric study based on Mach number (M), mass loading (Φ_m) and Stokes number (St) are provided in § 4. This is followed by an analysis of the mechanisms of local pressure intensity changes in the turbulence using the transport budget derived in § 2. The effect of particles on the near-field pressure characteristics are then provided. Finally, the results are summarized in § 5.

2. Pressure intensity transport in the presence of particles

In this study, mechanisms of pressure intensity changes are examined via a detailed analysis of a transport budget, which necessitates deriving a consistent Reynolds-averaged pressure intensity equation. Unlike in single-phase flows where the Navier–Stokes equations can be directly averaged to obtain a macroscopic description (i.e. a model for the mean flow), special care needs to be taken for turbulent multiphase flows. As discussed in Fox (2014), averaging the microscale equations (a model that solves the Navier–Stokes equation for the fluid with appropriate boundary conditions at the two-phase interface), omits important interphase coupling terms (e.g. Capecelatro *et al.* 2015). As such, deriving the averaged equations starting from a mesoscale description retains physics by explicitly accounting for volume fraction and interphase coupling terms. In this section, the volume-filtered compressible flow equations are presented and are used to derive the pressure intensity transport that explicitly include multiphase effects.

2.1. *A mesoscale description for compressible two-phase flows*

To arrive at a mesoscale description for compressible particle-laden flows, the Navier–Stokes equations are split into microscale processes that take place on the scale of a particle and below, and meso- to macroscale processes that take place on a scale much larger than the particle size. Anderson & Jackson (1967) provide such a basis for this approach by applying a local volume filtering operator to the incompressible Navier–Stokes equations, thereby replacing the point variables (fluid velocity, pressure, etc.) by filtered fields. Applying a similar approach to the viscous compressible Navier–Stokes equations, the volume-filtered conservation equations can be expressed as (see appendix A for details)

$$\frac{\partial \alpha\rho}{\partial t} + \nabla \boldsymbol{\cdot} (\alpha\rho\boldsymbol{u}) = 0, \tag{2.1}$$

$$\frac{\partial \alpha\rho\boldsymbol{u}}{\partial t} + \nabla \boldsymbol{\cdot} (\alpha\{\rho\boldsymbol{u}\otimes\boldsymbol{u} + p\mathbb{I} - \boldsymbol{\tau}\}) = (p\mathbb{I} - \boldsymbol{\tau}) \boldsymbol{\cdot} \nabla\alpha + \boldsymbol{F}, \tag{2.2}$$

and

$$\frac{\partial \alpha\rho E}{\partial t} + \nabla \boldsymbol{\cdot} \alpha(\{\rho E + p\}\boldsymbol{u} - \boldsymbol{u}\boldsymbol{\cdot}\boldsymbol{\tau}) + \alpha\nabla\boldsymbol{\cdot}\boldsymbol{q} = (\boldsymbol{\tau} - p\mathbb{I}) : \nabla(\alpha_p\boldsymbol{u}_p) + \boldsymbol{u}_p \boldsymbol{\cdot} \boldsymbol{F}, \tag{2.3}$$

where α is the fluid-phase volume fraction, ρ is the fluid density, $\boldsymbol{u}$ the fluid velocity, $\boldsymbol{u}_p$ is the particle-phase velocity (in an Eulerian frame of reference) and E the total energy. Interphase heat transfer (based on the flow configuration in § 3) had negligible effect on the results and is neglected here. Flow variables in equations (2.1)–(2.3) have been non-dimensionalized by ambient density $\rho^\star_\infty$, speed of sound $c^\star_\infty$, a characteristic length scale $L^\star$ (based on vorticity thickness defined in equation (3.3)) and heat capacity at constant pressure $C^\star_p$. Dimensional quantities are denoted by a superscript $\star$, and the subscript ∞ indicates reference quantities (taken to be air). The source term $\boldsymbol{F}$ appearing in equations (2.2) and (2.3) accounts for momentum coupling between the particle and gas phases, and its form will be discussed in § 3.2. The non-dimensional viscous stress tensor is given by

$$\boldsymbol{\tau} = \frac{\mu}{Re_c}(\nabla\boldsymbol{u} + \nabla\boldsymbol{u}^{\mathrm{T}}) + \frac{\lambda}{Re_c}\nabla\boldsymbol{\cdot}\boldsymbol{u} \tag{2.4}$$

and the heat flux $\boldsymbol{q}$ is

$$\boldsymbol{q} = -\frac{\mu}{Re_c Pr}\nabla T, \tag{2.5}$$

where $Pr \equiv C^\star_p\mu^\star/k^\star = 0.7$ is the Prandtl number, with $\mu^\star$ and $k^\star$ the dynamic viscosity and thermal conductivity, respectively. The Reynolds number used in the formulation is defined as $Re_c = Re/M$, where $Re = \rho^\star_\infty \Delta U^\star L^\star/\mu^\star_\infty$ is the flow Reynolds number with $\Delta U^\star$ a characteristic velocity defined later, and $M = \Delta U^\star/c^\star_\infty$ is the Mach number. The non-dimensional viscosity is modelled as a power law $\mu = [(\gamma - 1)T]^n$, with $n = 0.666$ as a model for air and $\gamma = 1.4$ is the ratio of specific heats. The second coefficient of viscosity is given by $\lambda = \mu_B - \frac{2}{3}\mu$, where the bulk viscosity $\mu_B = 0.6\mu$ is chosen as a model for the bulk viscosity of air. Assuming an ideal gas, the thermodynamic pressure and temperature depend on

$$p = (\gamma - 1)(\rho E - \tfrac{1}{2}\rho\boldsymbol{u}\boldsymbol{\cdot}\boldsymbol{u}) \tag{2.6}$$

and

$$T=\frac{\gamma p}{\rho(\gamma-1)}. \tag{2.7}$$

Since pressure is a key observable in the simulations, its transport equation is useful for examining the competition of the mechanisms generating it. Differentiating equation (2.6) with respect to time and substituting equations (2.1)–(2.3) yields the pressure evolution equation in the presence of a disperse phase,

$$\frac{\mathrm{D}p}{\mathrm{D}t}=-\gamma p\nabla\boldsymbol{\cdot}\boldsymbol{u}+\mathcal{D}-\gamma p\frac{\mathrm{D}\ln\alpha}{\mathrm{D}t}+\frac{\gamma-1}{\alpha}(\boldsymbol{u}_p-\boldsymbol{u})\boldsymbol{\cdot}\boldsymbol{F}, \tag{2.8}$$

where $\mathrm{D}/\mathrm{D}t=\partial/\partial t+\boldsymbol{u}\boldsymbol{\cdot}\nabla$ is the material derivative operator and terms involving molecular transport effects are combined into

$$\mathcal{D}=\frac{\gamma-1}{\alpha}(\boldsymbol{\tau}:\nabla\alpha\boldsymbol{u}+\boldsymbol{\tau}:\nabla\alpha_p\boldsymbol{u}_p)+\gamma\nabla\boldsymbol{\cdot}\frac{\mu}{Re_c\,Pr}\nabla(p/\rho). \tag{2.9}$$

Compared to the single-phase pressure transport equation (e.g. Pantano & Sarkar 2002), the last two terms on the right-hand side of equation (2.8) represent new contributions due to the presence of particles. The second-to-last term on the right-hand side involves convection aligned with volume fraction gradients as well as a mechanism associated with the so-called *pDV* work term (Lhuillier, Theofanous & Liou 2010). The last term on the right-hand side represents work due to drag which is only active when the slip velocity magnitude between the phases is $|\boldsymbol{u}_p-\boldsymbol{u}|>0$.

2.2. *Averaged pressure intensity*

For examining mechanisms affecting the pressure intensity in turbulence, we use Reynolds decomposition with spatial averaging operator $\overline{(\cdot)}$, such that any quantity A can be decomposed into $A=\overline{A}+A'$ as is often used to examine Reynolds stress or turbulent kinetic energy transport.

Using this decomposition, multiplying equation (2.8) by p and rearranging yields the following pressure intensity transport equation

$$\begin{aligned}\frac{\partial\overline{p'p'}}{\partial t}+\overline{\boldsymbol{u}}\boldsymbol{\cdot}\nabla\overline{(p'p')}=&-2\gamma\overline{p}\ \overline{p'\nabla\boldsymbol{\cdot}\boldsymbol{u}'}-(2\gamma-1)\overline{p'p'\nabla\boldsymbol{\cdot}\boldsymbol{u}'}\\&-2\overline{\boldsymbol{u}'p'}\boldsymbol{\cdot}\nabla\overline{p}-\nabla\boldsymbol{\cdot}(\overline{p'p'\boldsymbol{u}'})-2\gamma\overline{p'p'}\nabla\boldsymbol{\cdot}\overline{\boldsymbol{u}}+\underbrace{2\overline{p'\mathcal{D}'}}_{\text{viscous and heat conduction}}\\&\times\underbrace{-2\gamma\left(\overline{p'p'\frac{\mathrm{D}\ln(\alpha)}{\mathrm{D}t}}+\overline{p}\ \overline{p'\frac{\mathrm{D}\ln(\alpha)}{\mathrm{D}t}}\right)}_{\text{volume displacement}}\\&+\underbrace{2(\gamma-1)\left(\overline{\frac{p'\boldsymbol{F}}{\alpha}}\boldsymbol{\cdot}(\overline{\boldsymbol{u}_p}-\overline{\boldsymbol{u}})+\overline{\frac{p'\boldsymbol{F}}{\alpha}\boldsymbol{\cdot}(\boldsymbol{u}'_p-\boldsymbol{u}')}\right)}_{\text{drag coupling}}.\end{aligned} \tag{2.10}$$

The first two lines of equation (2.10) have the same form as for single-phase flows, and they have been analysed for several turbulence configurations (e.g. Sarkar 1992).

As shown by Sarkar (1992), $\overline{p'\nabla\cdot\boldsymbol{u}'}$ acts to transfer energy between the kinetic and internal energy of turbulence. The term $\nabla\cdot\overline{(p'p'\boldsymbol{u})}$ has a turbulent-flux-like form for pressure intensity, $-2\gamma\overline{p'p'}\nabla\cdot\bar{\boldsymbol{u}}$ has a production-like form for pressure intensity, although depending on mean flow expansion rather than mean shear, and $2\overline{p'\mathcal{D}'}$ combines all of the heat conduction and viscous mechanisms based on (2.9). The terms involving $\mathrm{D}/\mathrm{D}t(\ln\alpha)$ show how pressure intensity is modified from the material transport of volume fraction (depending on its correlation to the local pressure) and the last term describes the effects due to drag. The analysis of equation (2.10) in subsequent sections focuses on groups of terms: (i) volume displacement; (ii) drag coupling; (iii) viscous and heat conduction; and (iv) remaining terms without $\overline{(p'p')}_t$ that comprise what we call the inviscid hydrodynamics. The following sections introduce the simulations used in evaluating the terms in (2.10); their relative importance on modifying pressure fluctuations will be presented in § 4.2.

3. Simulation details

3.1. *Flow configuration*

The simulations are designed to provide a model flow to represent phenomenology of full-scale droplet-injected jet applications. To this end, we focus on what can be considered the near-nozzle exit region of a high-speed shear layer. Assuming the turbulent mixing layers from these jet exits are thin relative to their curvature, the turbulence would develop similarly as a planar spatially developing shear layer. Using a coordinate transformation based on the mean streamwise flow, we consider the temporally developing frame of reference, as shown in figure 1. Focusing on the thin shear layer turbulence enables the direct simulation of a broader range of turbulence scales than could be represented in a full jet simulation; the largest scales there being the size of the jet diameter rather than the shear layer thickness. Thus, the present configuration provides a Reynolds-number realistic representation of a section of a high-Reynolds-number jet, and it enables probing of the sound generation mechanisms of high-Reynolds-number turbulence. We mention that the acoustic far field from the current mixing layers will not include any geometric propagation associated with that from a round jet nor from the closing of shear layers at the end of the potential core. For the very near-field analysis considered here (i.e. within $20\,\delta_m$ where the momentum thickness δ_m is given in equation (3.2)), results are expected to compare well with those near jets. One such comparison was made between temporally developing shear layer direct numerical simulation and round jet large-eddy simulation (LES) which showed similar pressure skewness S_k with Mach number (Buchta & Freund 2017). Although such a configuration precludes a one-to-one comparison to far-field jet sound, it provides a detailed description of underlying particle–turbulence and acoustic interactions and motivates analysis for more complex configurations.

In practice, water droplets are introduced into the jet exit shear layers by water-jet injection ports positioned azimuthally near the nozzle exit (Krothapalli *et al.* 2003; Greska 2005), which would be challenging to consider in the planar temporally developing configuration here. However, experimental measurements (Krothapalli *et al.* 2003) indicate that the injected liquid breaks up quickly in the high-speed shear layer and forms a cloud of small droplets (mainly $d_p < 5\ \mu\mathrm{m}$) at the end of the injection region where turbulence attenuation is observed. Therefore, by seeding particles directly inside developed turbulence, focus is placed on turbulence–particle coupling mechanisms, multiphase development in a compressible regime and near-field sound

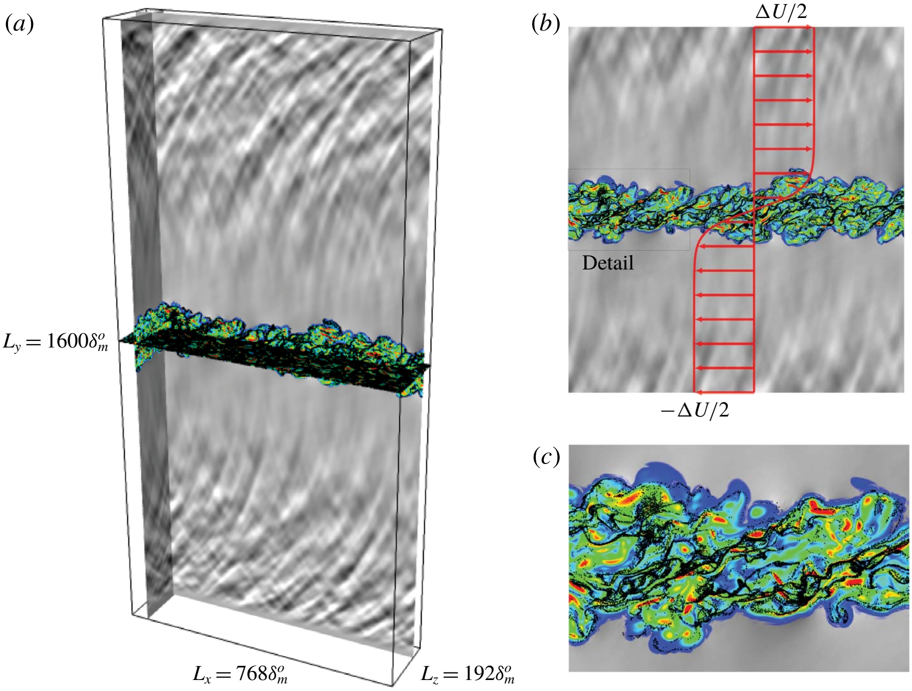

FIGURE 1. (Colour online) Shear layer configuration: (*a*) iso-view of the computational domain, (*b*) zoomed-in view of the *x*–*y* plane and (*c*) detail of (*b*). The vorticity magnitude is coloured by $(\boldsymbol{\nabla} \times \boldsymbol{u}) < 0.5\Delta U/\delta_m$ increasing from blue to red with particle position in black. Grey scales of dilatation are from $|\boldsymbol{\nabla} \boldsymbol{\cdot} \boldsymbol{u}| < 0.01\Delta U/\delta_m$ decreasing from black to white.

changes under such conditions. Future work may be warranted to assess how the current turbulence–particle–acoustic coupling generalizes to other injection–turbulence interactions and for evaporation in heated jets.

The gas phase is initialized with velocity

$$[u, v, w](\boldsymbol{x}) = \left[\frac{\Delta U}{2} \tanh\left(\frac{y}{2\delta_m^o}\right) + u'(\boldsymbol{x}), v'(\boldsymbol{x}), w'(\boldsymbol{x})\right], \tag{3.1}$$

with ΔU the velocity difference between the upper and lower streams and velocity perturbations $([u'(\boldsymbol{x}), v'(\boldsymbol{x}), w'(\boldsymbol{x})])$ are comprised of a broadband Fourier based form localized in the shear layer. Details of the additive perturbations used for triggering turbulence are explained in full elsewhere (Capecelatro & Buchta 2017). The initial pressure is assumed constant and density is computed from the Crocco–Busemann relationship, which is an established initialization of similar shear layer turbulence simulations (Vishnampet, Bodony & Freund 2015; Buchta & Freund 2017).

For each simulation presented herein, the domain lengths in the *x* (streamwise), *y* (cross-stream) and *z* (spanwise) directions are $L_x = 768\delta_m^o$, $L_y = 1600\delta_m^o$ and $L_z = 128\delta_m^o$ with $768 \times 1601 \times 192$ grid points, respectively, based on the initial momentum thickness (δ_m^o) using

$$\delta_m(t) = \frac{1}{\rho_\infty \Delta U^2} \int_{-Ly/2}^{L_y/2} \overline{\rho} \left[\frac{1}{2}\Delta U - \widetilde{u}(y, t)\right] \left[\frac{1}{2}\Delta U + \widetilde{u}(y, t)\right] \mathrm{d}y, \tag{3.2}$$

evaluated at $t = 0$. Tests indicated that near-field pressure fluctuations of the single-phase (unladen) case were independent of the domain size; moreover, they are similar to those parameters used in previous single-phase shear layer direct numerical simulations (DNS) (Buchta 2016; Buchta & Freund 2017). The Reynolds number based on the velocity difference and the initial momentum thickness is set to $Re_{\delta_m^o} = 120$. Turbulence spectra discussed in § 4.1 support a sufficient grid for resolving turbulence based on this initial Reynolds number. To model water droplets in air, the particle density is taken to be $\rho_p = 1000\,\rho_\infty$. The particle diameter, d_p, is then chosen to yield a desired initial Stokes number $St = \tau_p/\tau_f$ based on the particle and fluid time scales, $\tau_p = \rho_p d_p^2/(18\mu)$ and $\tau_f = \delta_\omega/\Delta U$, respectively. The fluid time scale τ_f is based on the vorticity thickness of the shear layer

$$\delta_\omega(t) = \frac{\Delta U}{|\mathrm{d}\tilde{u}(y, t)/\mathrm{d}y|_{max}}, \tag{3.3}$$

with $\tilde{u}(y, t)$ the Favre-average streamwise velocity. For the majority of the simulations, the initial Stokes number is set to $St = 1.0$. Sensitivity to Stokes number for $0.25 \leqslant St \leqslant 4$ is also examined for $M = 1.5$. The Stokes number based on the Kolmogorov time scale (τ_η), $St_\eta = \tau_p/\tau_\eta$, is in the range $3.4 \leqslant St_\eta \leqslant 4.4$ (for $St = 1$) at the time of particle seeding, where τ_η depends on the local dissipation rate in the shear layer. For reference, the Stokes number for the water-droplet injection in high-speed jets, based on $10\,\delta_w^o$ and $d_p = 4$ μm, was estimated to be 0.2 (Krothapalli *et al.* 2003). Initially, all of the simulations developed from vorticity thickness $\delta_w^o \equiv \delta_w(t = 0) = 1$, based on equations (3.1) and (3.3), to thickness $\delta_w(t = t^\bullet) \approx 10$, which was sufficient time to establish turbulence; at this time, $t = t^\bullet$, the particles were positioned inside the shear layer as previously described in Capecelatro & Buchta (2017). Rather than add particles at $t = 0$, which can affect turbulence transition, seeding them in turbulence is similar to micro-jet injection application for high-Reynolds-number full-scale jets. The total number of particles considered in each simulation is based on the volume fraction Φ_v within the shear layer, defined as

$$\Phi_v = \frac{N_p \pi d_p^3}{6 L_x L_z \delta_\omega^o}. \tag{3.4}$$

A summary of relevant parameters used in each case is provided in table 1. Across all of the laden simulations considered, the total number of particles varies in the range $3 \times 10^6 \lesssim N_p \lesssim 250 \times 10^6$ depending on mass loading and Stokes number. The corresponding mass loading within the shear layer

$$\Phi_m = \frac{\rho_p}{\rho} \frac{\Phi_v}{1 - \Phi_v}, \tag{3.5}$$

ranges from $\Phi_m = 0.1$ to 10. Most of the statistics reported throughout § 4 will concentrate on $\Phi_m = 0$, 1 and 10 for clarity. However, results for intermediate mass loadings will be included to highlight intermediate behaviour especially regarding sound intensity and TKE reduction.

3.2. *Particle-phase description*

In this work we consider monodisperse, spherical, rigid particles with diameters smaller than the Kolmogorov length scale. The displacement of an individual particle i

M	St	$St_\eta^\bullet$	$d_p/\eta^\bullet$	Φ_m	$N_p \times 10^6$
0.9	—	—	—	0.0	0
1.5	—	—	—	0.0	0
2.5	—	—	—	0.0	0
0.9	1.00	4.4	0.28	0.1	2.5
1.5	1.00	4.0	0.26	0.1	2.5
2.5	1.00	3.4	0.22	0.1	2.5
0.9	1.00	4.4	0.28	0.5	13
1.5	1.00	4.0	0.26	0.5	13
2.5	1.00	3.4	0.22	0.5	13
0.9	1.00	4.4	0.28	1.0	25
1.5	1.00	4.0	0.26	1.0	25
2.5	1.00	3.4	0.22	1.0	25
0.9	1.00	4.4	0.28	2.0	50
1.5	1.00	4.0	0.26	2.0	50
2.5	1.00	3.4	0.22	2.0	50
0.9	1.00	4.4	0.28	10	250
1.5	1.00	4.0	0.26	10	250
2.5	1.00	3.4	0.22	10	250
1.5	0.25	1.0	0.13	1.0	70
1.5	4.00	16.0	0.51	1.0	3.1

TABLE 1. Simulation configurations and corresponding initial fluid–particle parameters. The superscript '$\bullet$' corresponds to the particle introduction time when the shear layer growth reaches $\delta_m/\delta_m^o = 10$. The Kolmogorov length scale at this time ($\eta^\bullet$) is computed from midplane ($y = 0$) turbulence data.

is calculated according to Newton's second law of motion by

$$\frac{\mathrm{d}\boldsymbol{x}_p^{(i)}}{\mathrm{d}t} = \boldsymbol{v}_p^{(i)}, \tag{3.6}$$

and

$$\frac{\mathrm{d}\boldsymbol{u}_p^{(i)}}{\mathrm{d}t} = \frac{\boldsymbol{f}_{drag}^{(i)}}{m_p} - \frac{1}{\rho_p}\nabla p[\boldsymbol{x}_p^{(i)}] + \frac{1}{\rho_p}\nabla \boldsymbol{\cdot} \boldsymbol{\tau}[\boldsymbol{x}_p^{(i)}], \tag{3.7}$$

where $\boldsymbol{x}_p^{(i)}$ and $\boldsymbol{v}_p^{(i)}$ are the instantaneous position and velocity of the ith particle, respectively, and m_p is the particle mass. Here, the fluid-phase velocity, pressure gradient and viscous stress tensor are taken at the centre position of particle i. The particle equations are non-dimensionalized using the same reference quantities used in equations (2.1)–(2.3). The drag force is given by

$$\frac{\boldsymbol{f}_{drag}^{(i)}}{m_p} = \frac{\alpha}{\tau_p}(\boldsymbol{u}[\boldsymbol{x}_p^{(i)}] - \boldsymbol{v}_p^{(i)})F(\alpha, Re_p), \tag{3.8}$$

where F is the dimensionless drag force coefficient of Tenneti, Garg & Subramaniam (2011), which has a nonlinear dependence on the particle Reynolds number $Re_p = \rho d_p Re_c \|\boldsymbol{u} - \boldsymbol{v}_p\|/\mu$.

This drag coefficient reduces to the classic Schiller & Naumann (1933) correlation in the limit of small particle concentration, and reduces to Stokes drag as Re_p

approaches 0. For all simulations presented in this work, the particle Mach number and Knudsen number were found to be small (i.e. < 0.05 for particle Mach number), and thus compressibility effects on the drag force (e.g. Clift, Grace & Weber 2005) can be neglected. Other models for particle motion in compressible, inhomogeneous flows have been analysed (e.g. Parmar, Haselbacher & Balachandar 2012), which include important physical mechanisms for which compressible hydrodynamics couple to particle scales. Based on the current shear layer configuration, the primary energetic pressure wavelengths, for example, are $O(10^3)$ greater than the particle diameter, suggesting a scale separation (see figures 8 and 14). From high-speed shear layer turbulence, intense sound waves steepen (e.g. Lighthill (1956)) and form weak shocks that have shorter wavelength. This effect shrinks the scale separation, and the particle-phase description would need modified. However, in the current simulations, particles reside in the shear layer turbulence, $|y| \lesssim 3\delta_m$ (see figure 9) and such weak shock wave and particle interactions are absent.

The Basset force and added mass effects are neglected due to the large density ratios considered, which is appropriate when the particle diameter is significantly smaller than the acoustic wavelengths (Cleckler, Elghobashi & Liu 2012). It should also be noted that the current numerical approach precludes exact particle–acoustic interaction (e.g. acoustic scattering by solid bodies) since boundary conditions (e.g. no-slip condition) are not applied at the particle surface. Omitting these mechanisms are not anticipated to have large effect on the current results. Again, this is supported, to a degree, by the scale separation between particle diameter and hydrodynamic scales. For heated jets or shear layers, which are not considered here, other mechanisms like droplet evaporation and heat transfer between phases may contribute to changes in turbulence and sound radiation. However, the current configuration considers equal temperature between particles and the ambient gas phase; thus, these effects are also anticipated to be small and are therefore neglected.

Finally, all the reported results neglect particle collision effects. In the small volume fraction limit $\alpha_p \ll 1$, this approximation is reasonable, and it has been applied in similar shear layer turbulence configurations (Dai *et al.* 2018). However, for the largest mass loading considered here, $\Phi_m = 10$ with $\Phi_v = O(10^{-2})$, collisions are abundant. Despite this, numerical tests, including particle collisions, indicate a negligible statistical effect on the turbulence and near-field pressure radiation for coefficient of restitution in the range $0.2 \leqslant \mathrm{e} \leqslant 0.8$; thus, our conclusions appear insensitive to particle collisions. Different injection scenarios, higher Stokes numbers or a mixture of these with particle collisions may reveal a sound radiation sensitivity.

3.3. *Numerical implementation*

Spatial derivatives in equations (2.1)–(2.5) are approximated by high-order finite-difference operators that satisfy the summation-by-parts (SBP) property (Strand 1994). An explicit, sixth-order, centred finite difference is used in the domain interior, and third-order, one-sided finite differences are applied at the boundary. The SBP scheme is combined with the simultaneous-approximation-term (SAT) approach (Svärd, Carpenter & Nordström 2007; Vishnampet *et al.* 2015) at the lateral domain boundaries which provides provable stability. The outflow SAT at $\pm y = L_y/2$ employs a characteristic boundary condition that weakly enforces a stationary target solution $\boldsymbol{Q}_{target}(y) = \boldsymbol{Q}(y, t = 0)$, where $\boldsymbol{Q} = [\alpha\rho, \alpha\rho\boldsymbol{u}, \alpha\rho E]^{\mathrm{T}}$ is the vector of fluid-phase conserved variables. To assist in the asymptotic convergence of the SAT condition and further avoid spurious reflections into the domain, an additional sponge zone

(Freund 1997) of width $w = 50\delta_m^o$ is added to the flow equations (denoted $\mathcal{N}$ for brevity) according to

$$\mathcal{N}(\boldsymbol{Q}) = -\sigma(y)[\boldsymbol{Q} - \boldsymbol{Q}_{target}(y)]. \tag{3.9}$$

The sponge strength increases quadratically toward the domain extent by

$$\sigma(y) = \left(\frac{|y| - (L_y/2 - w)}{w}\right)^2. \tag{3.10}$$

Second derivative approximations apply first-order derivative operators consecutively, which necessitates using artificial dissipation to damp the highest wavenumber energetics supported by the grid. To this end, high-order accurate SBP dissipation operators are used to provide artificial dissipation which are based on the third derivative (Mattsson, Svärd & Nordström 2004; Vishnampet 2015). The fluid and particle equations, (2.1)–(2.3) and (3.6)–(3.7), are advanced in time with a constant time step using a standard fourth-order explicit Runge–Kutta scheme. The acoustic Courant–Friedrichs–Lewy (CFL) number was monitored throughout the simulation and remained below $\text{CFL} < 0.5$.

Fluid quantities appearing in equation (3.8) are interpolated to the location of each particle via trilinear interpolation. The interphase exchange terms appearing in equations (2.1) and (2.3) are computed by projecting the Lagrangian data onto the computational grid according to

$$\alpha = 1 - \alpha_p = 1 - \sum_{i=1}^{N_p} \mathcal{G}(|\boldsymbol{x} - \boldsymbol{x}_p^{(i)}|)V_p, \tag{3.11}$$

$$\boldsymbol{F} = -\sum_{i=1}^{N_p} \mathcal{G}(|\boldsymbol{x} - \boldsymbol{x}_p^{(i)}|)\boldsymbol{f}_{drag}^{(i)}, \tag{3.12}$$

and

$$\boldsymbol{u}_p \boldsymbol{\cdot} \boldsymbol{F} = -\sum_{i=1}^{N_p} \mathcal{G}(|\boldsymbol{x} - \boldsymbol{x}_p^{(i)}|)\boldsymbol{v}_p^{(i)} \boldsymbol{\cdot} \boldsymbol{f}_{drag}^{(i)}, \tag{3.13}$$

where $\mathcal{G}$ is a filter kernel, N_p is the total number of particles and V_p is the particle volume. In this work, $\mathcal{G}$ is taken to be Gaussian with a characteristic size $\delta_f = 10d_p$, defined as the full width at half the height of the kernel. For computational efficiency, the filtering procedure is solved in two steps (Capecelatro & Desjardins 2013). First, the particle data are transferred to the nearest neighbouring cells via trilinear extrapolation. The data are then diffused such that the final width of the filtering kernel is independent of the mesh size. To ensure unconditional stability and reduce computational cost, the diffusion process is solved implicitly during each Runge–Kutta sub-iteration by utilizing the approximate factorization scheme of Briley & McDonald (1977). When the particle diameter is sufficiently smaller than the grid spacing ($d_p < \Delta x/10$), the diffusion process is not considered and the projection method reverts to trilinear extrapolation. Details on the interphase exchange process can be found in (Capecelatro & Desjardins 2013).

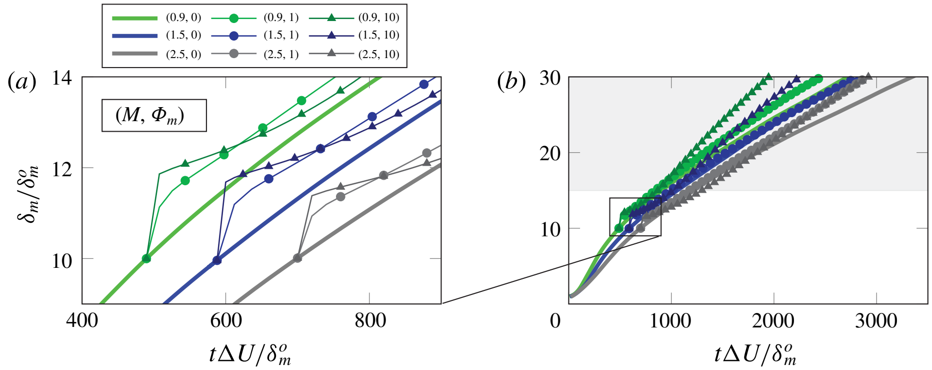

FIGURE 2. (Colour online) Shear layer growth (*a*) near the particle introduction time and (*b*) for the full simulation time. The shaded region in (*b*) indicates when the statistics are averaged based on δ_m. The number of time steps between symbols is approximately 300.

4. Results

Temporally developing shear flows, albeit representing a simpler configuration than jet turbulence, require some explanation for analysis of their time-dependent statistics. The averaging of simulation data takes place in two stages. First, discrete time data are averaged in the statistically homogeneous x- and z-directions either by Favre averaging (denoted by a tilde) or Reynolds averaging (denoted by an overbar). Symmetry is often invoked in the averaging above and below the shear layer (see figure 3 as an example). Second, unless otherwise indicated, the spatially averaged data are then time averaged in a self-similar coordinate $y/\delta_m(t)$ at discrete time intervals during the shear layer growth $15 \leqslant \delta_m/\delta_m^o \leqslant 30$. The conclusions reported in this section are unchanged for reduced time sampling, supporting a level of statistical convergence.

4.1. *Shear layer growth and turbulence*

Shear layer growth and dynamics near the particle introduction time are shown in figure 2. After an initial transient in the range $0 < t\Delta U/\delta_m^o \lesssim 1000$, the unladen ($\Phi_m = 0$) shear layers grow approximately linearly, indicating a level of self-similarity, and as expected from experiments (Elliott & Samimy 1990; Goebel & Dutton 1991; Debisschop, Chambres & Bonnet 1994) and previous simulations (Pantano & Sarkar 2002; Kleinman & Freund 2008) the growth decreases with increasing M. After loading the shear layers when $\delta_m/\delta_m^o \approx 10$, a short transient persists for approximately $100\delta_m^o/\Delta U$ (see figure 2*a*) before establishing an approximate linear growth in figure 2(*b*). We note that the transient associated with seeding particles is small relative to the full simulation and acoustic propagation. Based on the distance from the centre of the shear layer ($y = 0$) to the domain boundary ($y = \pm 200\delta_m^o$), it would take approximately $50\delta_m/c_\infty$ to expel any disturbance by the particles. Tests have indicated that initial perturbations from the particle seeding transients are over an order of magnitude smaller than the sound generated from the turbulence and thus are not expected to impact conclusions.

Particle loading modifies the average growth rate of the shear layers for they attain δ_m/δ_m^o earlier in time with steeper slopes (growth rate increases) as shown in figure 2(*b*). The effect appears more pronounced for $M = 0.9$ and 1.5 and $\Phi_m = 1$ and 10. Analysis by Vreman, Sandham & Luo (1996) for single-phase shear layers

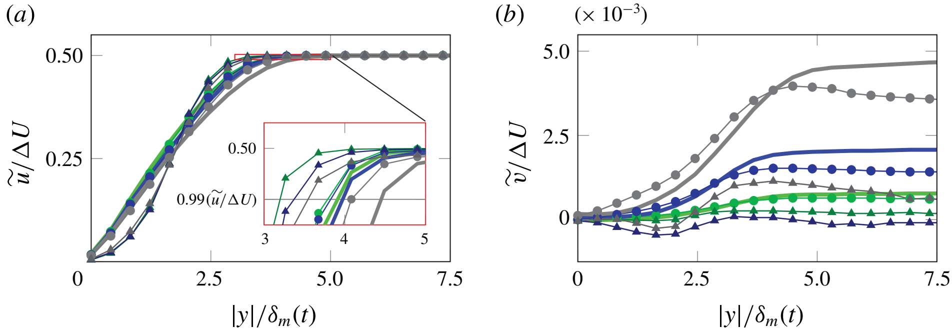

FIGURE 3. (Colour online) (*a*) Streamwise and (*b*) cross-stream average velocity. Antisymmetry of these profiles about the $y = 0$ plane has been used for the ensemble average in the similarity coordinate $|y|/\delta_m(t)$. The legend is the same as figure 2.

indicated that the growth rate is affected by cumulative effects of $\widetilde{u''v''}\,\partial\tilde{u}_y$ across the shear layer, for sufficiently high Reynolds number, where the double prime denotes a fluctuation about a Favre-averaged quantity. The mean flow in figure 3 shows modest changes for $\Phi_m \lesssim 1$. Yet for the largest mass loading, the mean streamwise velocity has a stronger velocity deficit for $|y|/\delta_m \lesssim 2$. This change in velocity shape has implications for the stability of the flow since the inflectional instability is fundamental to its development. However, these changes do not provide evidence for the increase in growth rates for which turbulence fluctuations are examined next.

Profiles of Reynolds stresses and TKE (figures 4 and 5) reveal that gas-phase velocity fluctuations are reduced by the addition of particles. The TKE within the mixing layer (at $y = 0$) is reduced by 70 %–78 % for $M = 0.9$ and 1.5 and less so for $M = 2.5$. For a fixed number of particles and comparing different Mach number, it might be anticipated that the particle–turbulence coupling effect at higher-speed flow might be subdued by its larger momentum. Reduction in the magnitude $\widetilde{u''v''}$, which is one mechanism, as previously mentioned, for affecting single-phase shear layer growth (Vreman *et al.* 1996), seems to contradict the changes in shear layer growth observed in figure 2. Thus, other particle–turbulence interactions, absent in the Vreman *et al.* (1996) analysis, such as volume displacement, must cause a rise in the growth rate of δ_m, especially at $\Phi_m = 10$, which motivates further analysis for mechanisms of multiphase compressible shear layer growth rates.

The turbulence for all of the simulations becomes broadband in the streamwise and spanwise directions as shown in figure 6. For the Mach numbers considered, particles act to reduce the energy across significant energy-containing length scales. This is consistent with TKE reduction observed in incompressible shear flow (Battista *et al.* 2018). Not unexpectedly, the particle-laden cases add energy into the highest wavenumbers $k\delta_m \gtrsim 40$ which has also been observed in other turbulence simulations (Gualtieri, Battista & Casciola 2017; Capecelatro *et al.* 2018).

To motivate further analysis of these interactions, visualizing the flow at the centreline of the mixing layer ($y = 0$), figure 7 shows preferential concentration of particles by the turbulence (i.e. accumulation in regions of low vorticity). Note that at $\delta_m/\delta_m^o = 10$ the particles were positioned randomly within the shear layer and have since migrated during the growth of the shear layers. Particle position relative to local vorticity magnitude and pressure fluctuations reveal a tendency for particles

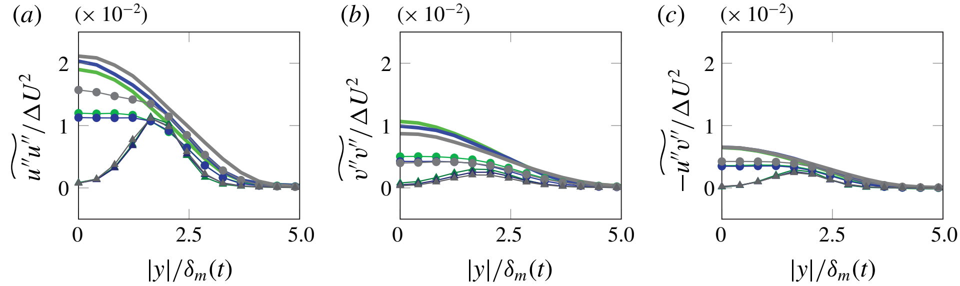

FIGURE 4. (Colour online) Reynolds stresses: (*a*) streamwise, (*b*) cross-stream (*c*) and streamwise normal. The line legend is the same as figure 2.

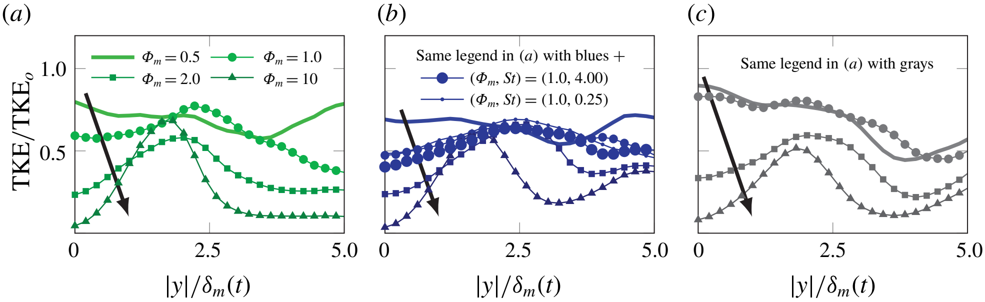

FIGURE 5. (Colour online) Mass loading effects on turbulent kinetic energy (relative to unladen cases) in the shear layers: (*a*) $M = 0.9$, (*b*) $M = 1.5$ and (*c*) $M = 2.5$. Stokes number effects are also included for $M = 1.5$ in (*b*). Arrows indicate increasing mass loading. All cases are $St = 1$ unless otherwise indicated.

to accumulate in low vorticity regions (high strain) and appear absent in the high vorticity, low pressure cores, as shown in figure 7(*c*). Based on the Stokes numbers considered here, this tendency is expected. Coupling between particles and pressure is also observed across similar length scales in figure 8 for $2 \lesssim k_x\delta_m \lesssim 20$ $(0.3 \lesssim l/\delta_m \lesssim 3)$, which show a pressure decrease compared to the $\Phi_m = 0$ case. Corresponding changes in the near-field sound (above the turbulence) are examined in the following section.

Average particle volume fraction, shown in figure 9, indicates a mass loading effect on the distribution of particles throughout the shear layer, and it is relatively insensitive to Mach number $0.9 \lesssim M \lesssim 2.5$. For $\Phi_m = 10$, there is higher relative concentration for $|y| < \delta_m$, while $\Phi_m = 1$ distributes the particles more evenly between $|y| \lesssim 3\delta_m$. This mass loading dependence on the concentration distribution may be a result of changes in the turbulence variation across the shear layer, since there is a significant decrease in TKE near the centreline in figure 5. Also, vorticity magnitude fluctuations decreases at $y = 0$ with increasing Φ_m for $0.9 \leqslant M \leqslant 2.5$ as shown in figure 10. Between $\Phi_m = 0$ and 1, the fluctuations decrease from $\approx 0.7\Delta U/\delta_m$ down to $|\boldsymbol{\nabla} \times \boldsymbol{u}|'_{rms} \approx 0.4\Delta U/\delta_m$, where 'r.m.s.' denotes root mean square. The highest mass loadings show an even larger deficit at $y = 0$. However, near the edges of the shear layers $(3 < |y|/\delta_m < 5)$, the vorticity fluctuations follow similar levels of unladen flows, which might be due, in part, to the majority of particles remaining close to the centreline $(|y|/\delta_m < 2)$ and less near the edges, as shown in figure 9 for $\Phi_m = 10$.

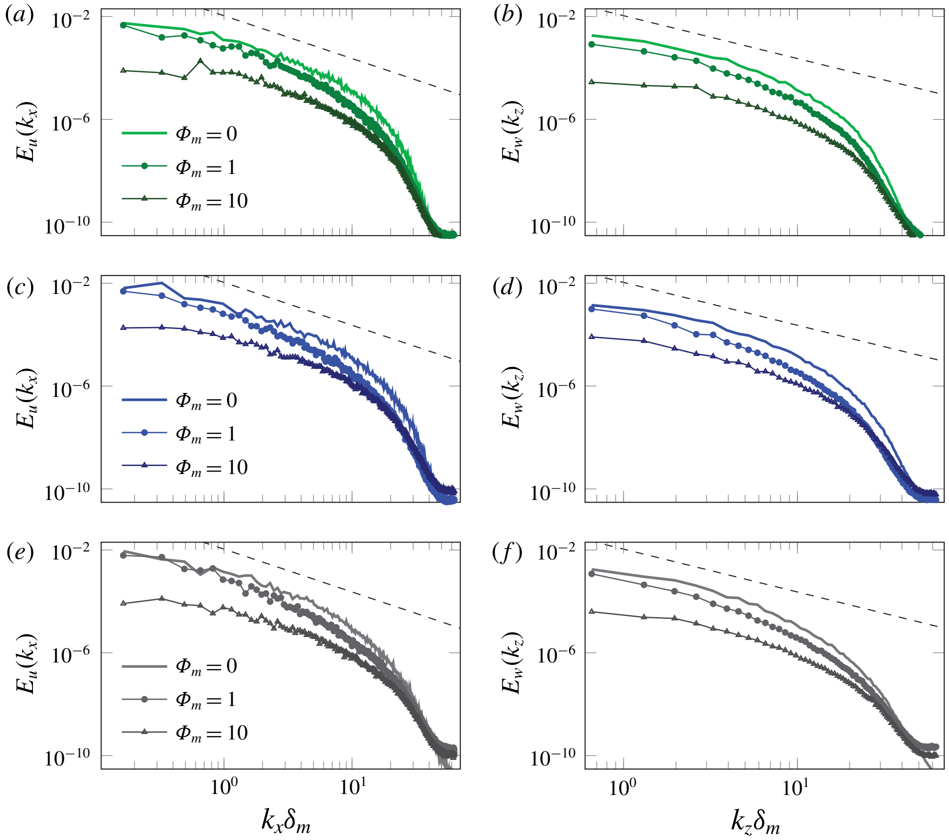

FIGURE 6. (Colour online) (*a*,*c*,*e*) Streamwise and (*b*,*d*,*f*) spanwise u- and w-velocity spectra, respectively, at $y = 0$ when $\delta_m/\delta_m^o = 20$: (*a*,*b*) $M = 0.9$, (*c*,*d*) $M = 1.5$ and (*e*,*f*) $M = 2.5$. The dashed line corresponds to a slope of $-5/3$. All spectral components are normalized by $\Delta U^2\delta_m$.

These observations support a turbophoresis effect for which particle concentration gradients are opposite in sign to turbulence gradients (Reeks 1983), suggesting a mode for particle migration.

4.2. *Local turbulence transport of p'_{rms}*

Combined terms of the pressure intensity budget introduced in § 2 are shown in figure 11. The terms have been grouped into their main physical mechanism for clarity. As discussed previously, the inviscid hydrodynamic coupling terms correspond to remaining terms not involved with molecular effects (e.g. momentum transport through viscosity), volume displacement effects or drag coupling through slip velocity. The average residual (which is the difference between the left and right sides of equation (2.10)) indicates the degree to which the intensity transport budget is accounted for, which is over an order of magnitude less than the largest contributors; thus its magnitude is immaterial to the conclusions here. Tests have indicated that these small imbalances are due, in part, to commutation of finite-difference derivatives and application of the chain rule to quantities that are not discretely transported.

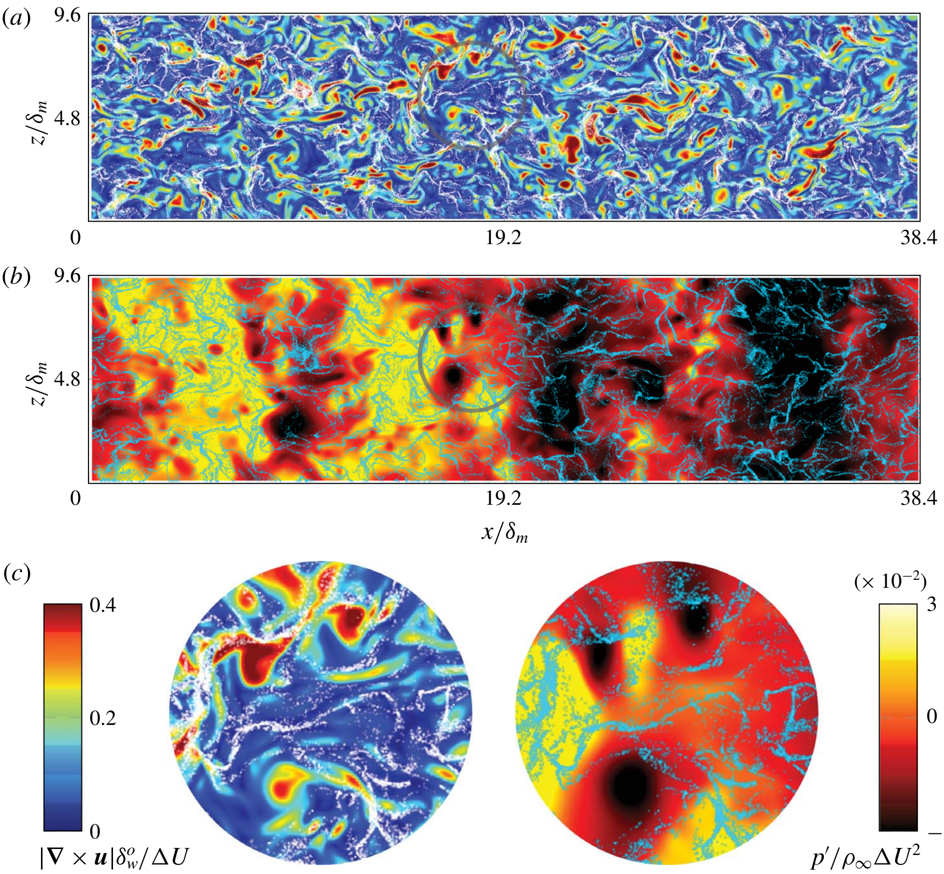

FIGURE 7. (Colour online) Visualization of the x–z plane for $M = 1.5$ at $y = 0$ when $\delta_m/\delta_m^o = 20$ for $\Phi_m = 1$: (*a*) vorticity magnitude coloured by $|\nabla \times \boldsymbol{u}|\delta_w^o/\Delta U < 0.4$ and particle positions are shown in white; (*b*) pressure fluctuations coloured from $-0.03 < p'/\rho_\infty \Delta U^2 < 0.03$ with particle position in blue; (*c*) enlarged regions as indicated in (*a*,*b*).

For the flows without particles ($\Phi_m = 0$), contributions from inviscid hydrodynamics play the largest role in the transport of pressure intensity, while molecular transport effects ($\mathcal{D}$) have a smaller effect, acting to reduce local pressure fluctuations. Similarly, for $(M, \Phi_m) = (0.9, 10)$, changes to $\overline{(p'p')}_t$ are due to changes in the turbulence (and its inviscid hydrodynamics) and not from the local sources and sinks that directly arise from particle coupling (i.e. volume displacement and drag). Drag coupling produces a large sink that approximately cancels the source by volume displacement in figure 11(*c*). For $M = 2.5$, the volume displacement effect is attenuated. For fixed number of particles across the M simulations, the time rate of change of volume fraction does not increase with M. However, the drag coupling in $M = 2.5$ remains a large factor due an increase in average slip velocity with larger ΔU.

4.3. *Near-field pressure fluctuations*

Sound fields and turbulence of laden and unladen simulations are shown in figure 12. As the Mach number increases, the waves above the turbulence (depicted with

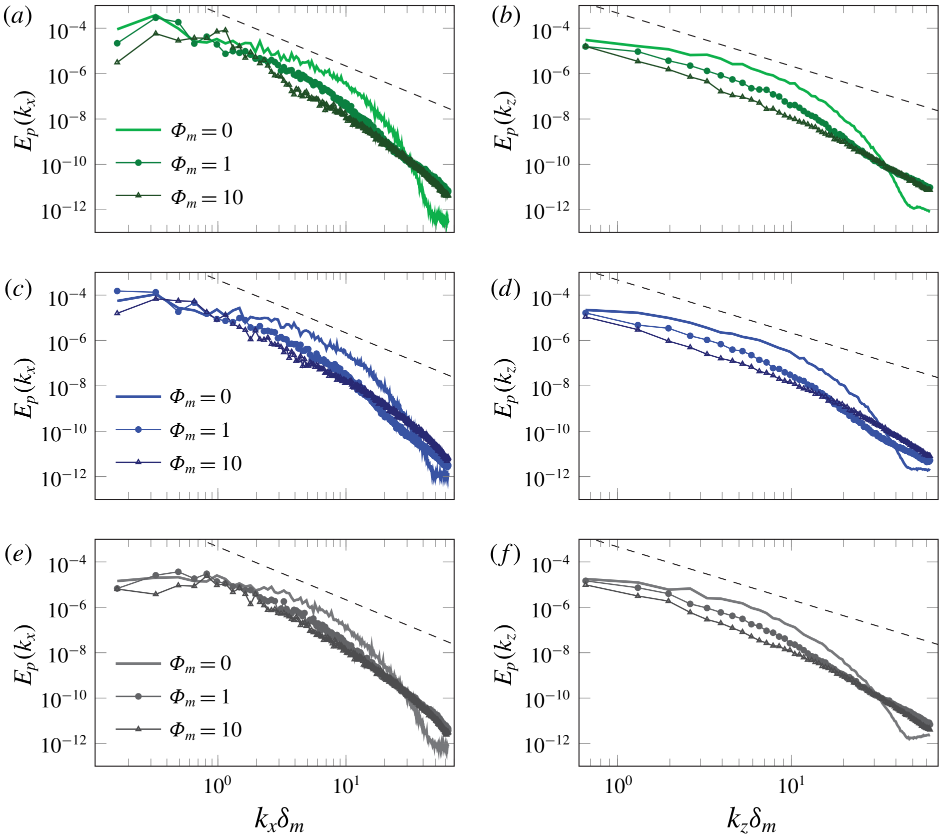

FIGURE 8. (Colour online) (a,c,e) Streamwise and (b,d,f) spanwise pressure spectra, respectively, at $y = 0$ when $\delta_m/\delta_m^o = 20$: (a,b) $M = 0.9$, (c,d) $M = 1.5$ and (e,f) $M = 2.5$. The dashed line corresponds to a slope of $-7/3$. All spectral components are normalized by $\Delta U^4 \rho_\infty^2 \delta_m$.

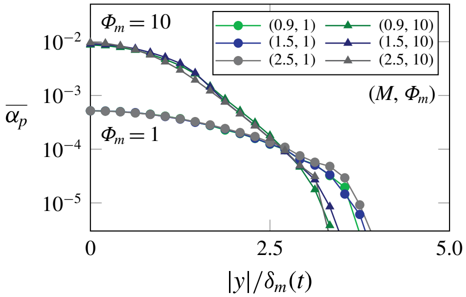

FIGURE 9. (Colour online) Average particle volume fraction through the shear layers for the intermediate $\Phi_m = 1$ and largest $\Phi_m = 10$ mass loadings.

$\nabla \cdot \boldsymbol{u}$) are more intense. For supersonic flows, the waves appear sharper and angled, consistent with Mach wave radiation (Phillips 1960; Laufer 1961; Ffowcs Williams & Maidanik 1965). For similar single-phase temporally developing shear layers, wave angle statistics with M have been quantified elsewhere (Buchta & Freund 2017).

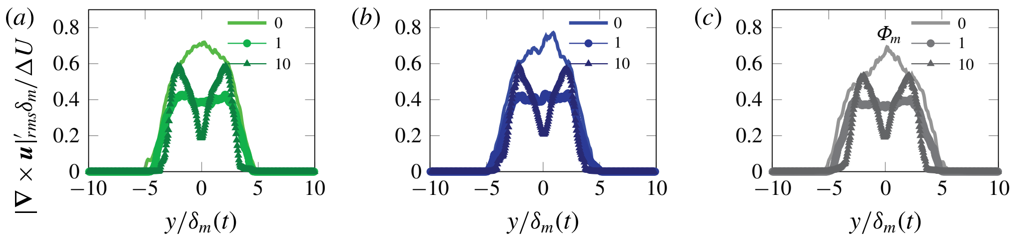

FIGURE 10. (Colour online) Root mean square of vorticity magnitude fluctuation when the $\delta_m/\delta_m^o = 20$: (*a*) $M = 0.9$, (*b*) $M = 1.5$ and (*c*) $M = 2.5$.

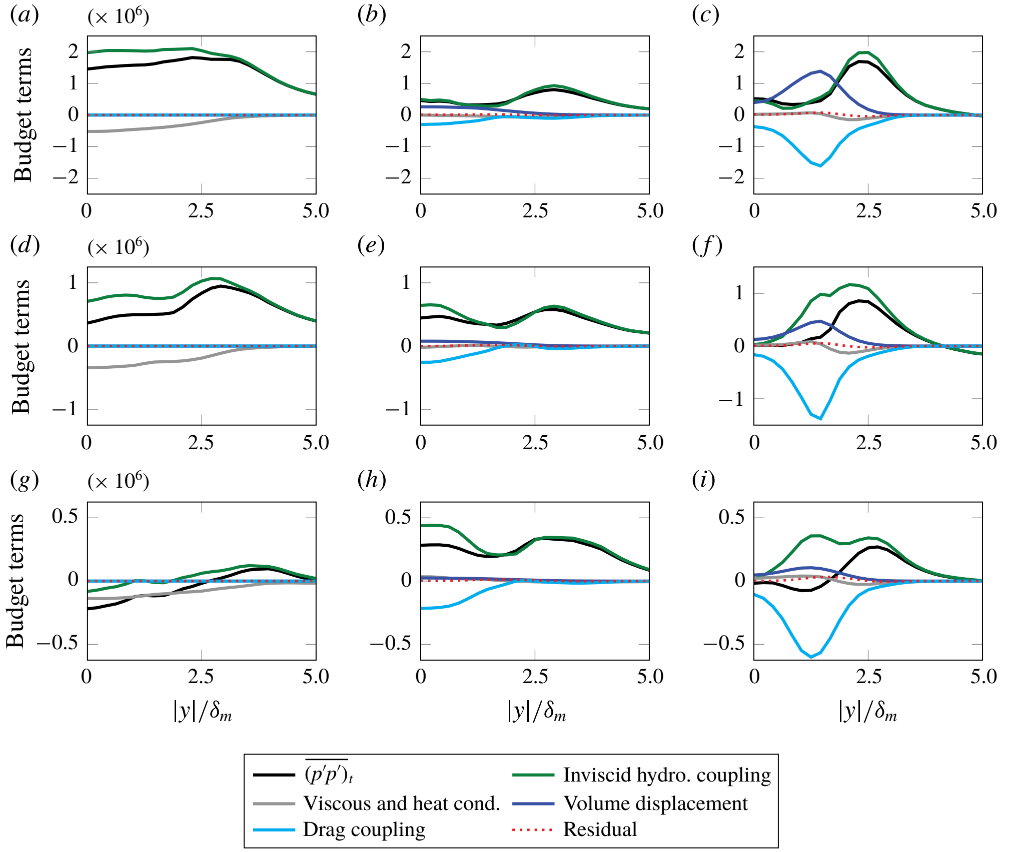

FIGURE 11. (Colour online) Mechanisms of pressure intensity transport: (*a–c*) $M = 0.9$, (*d–f*) $M = 1.5$ and (*g–i*) $M = 2.5$ for (*a*,*d*,*g*) $\Phi_m = 0$, (*b*,*e*,*h*) $\Phi_m = 1$ and (*c*,*f*,*i*) $\Phi_m = 10$. All components have been scaled by $\delta_w^o/(\rho_\infty^2 \Delta U^5)$. Note the *y*-scale changes with respect to Mach number.

For $M \gtrsim 1.5$ and $\Phi_m = 1$, the waves above the turbulence ($y \lesssim 10\delta_m$) are fewer and appear smoother than $\Phi_m = 0$. Changes in the vorticity magnitude are also apparent and show a decrease with particle loading, which is quantified in figure 10.

Sound field changes are likewise shown by instantaneous, pressure fluctuations in figure 13. The subsonic case $(M, \Phi_m) = (0.9, 10)$ shows a large increase in amplitude

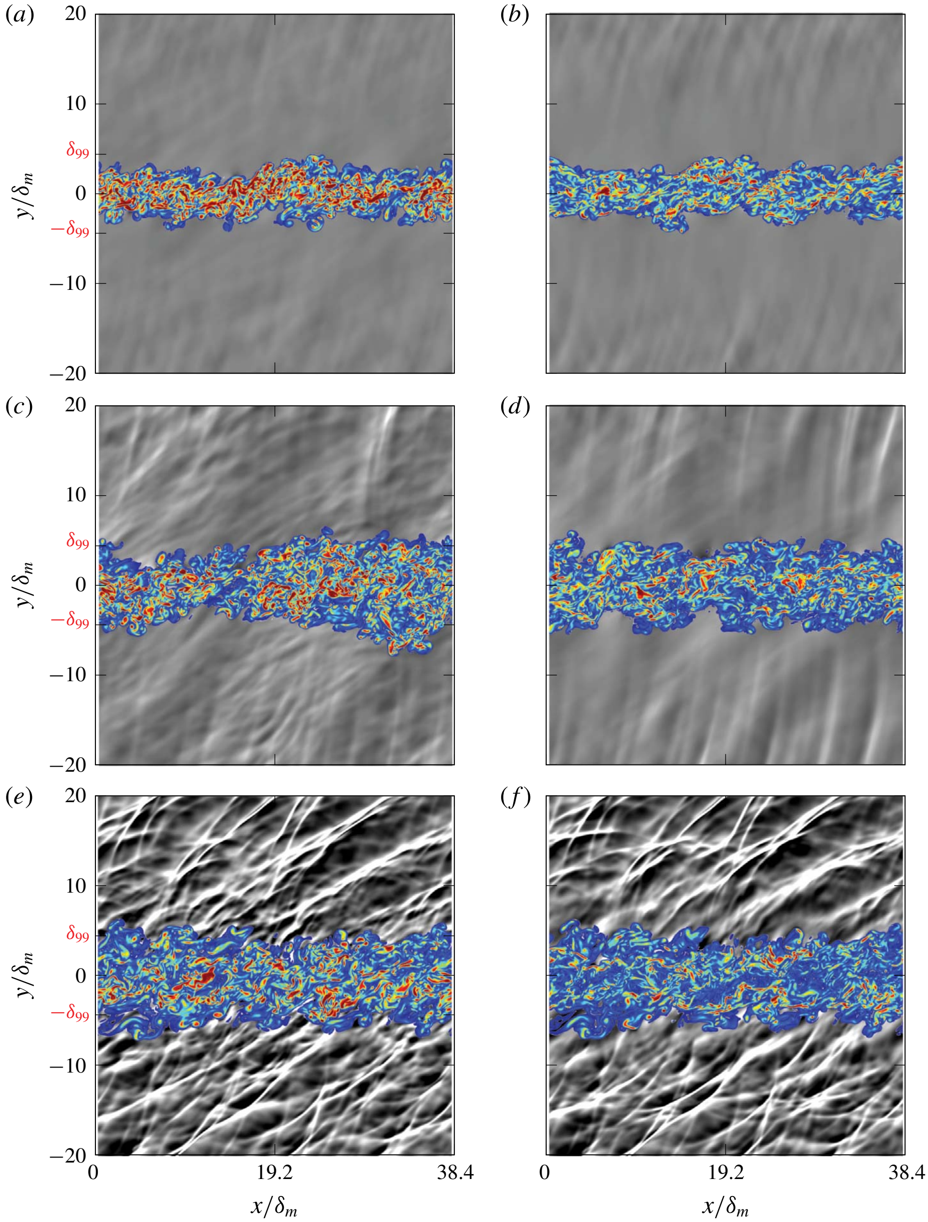

FIGURE 12. (Colour online) Dilatation (greys) shown in the range $-0.005 < \nabla \cdot \boldsymbol{u}\delta_w^o/\Delta U < 0.005$ and vorticity magnitude (colour) in the range $|\nabla \times \boldsymbol{u}|\delta_w^o/\Delta U < 0.4$ at $z = L_z/2$ mid-plane for $\varPhi_m = 0$ (*a*,*c*,*e*) and $\varPhi_m = 1$ (*b*,*d*,*f*) when $\delta_m/\delta_m^o = 20$. Unladen (left) and laden (right), with Mach number increasing from top to bottom: (*a*,*b*) $M = 0.9$, (*c*,*d*) $M = 1.5$ and (*e*,*f*) $M = 2.9$. Compressions, $\nabla \cdot \boldsymbol{u} < 0$, are shown in white. To highlight turbulence changes between left and right columns, particle positions are omitted in (*b*,*d*,*f*), and approximately one third of the full y-domain is shown.

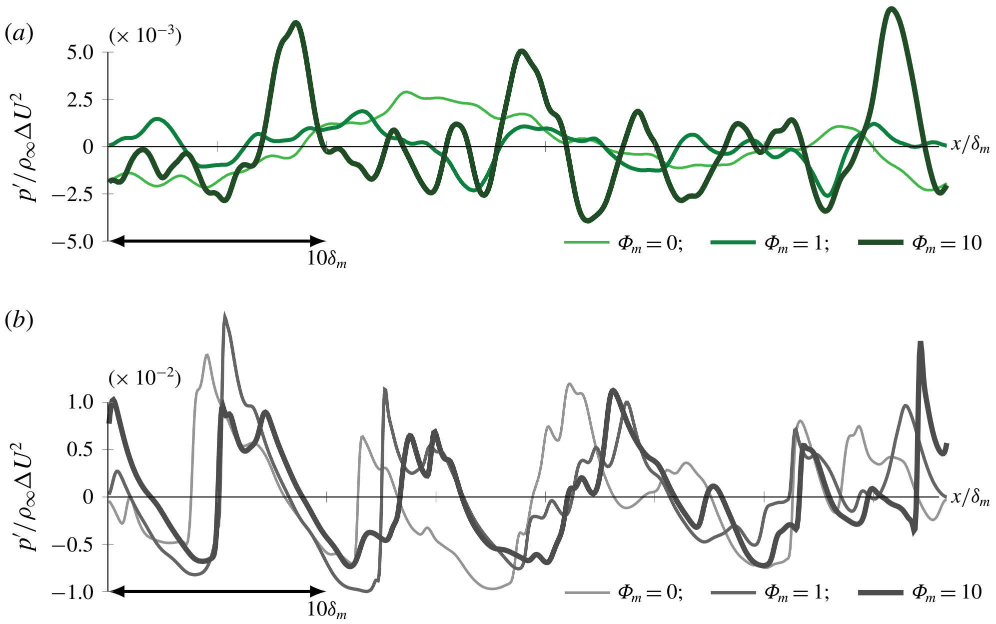

FIGURE 13. (Colour online) Mass loading effects on pressure variation in x for the subsonic and supersonic shear layers at $(y, z) = (15, 0)\,\delta_m$ when (*a*) $\delta_m/\delta_m^o = 20$ for $M = 0.9$ and when (*b*) $\delta_m/\delta_m^o = 30$ for $M = 2.5$.

and appears at shorter wavelengths. For $M = 2.5$, the largest pressure peaks near the shock-like waves appear to decrease. These observations in the pressure trace concur with spectral changes that will be examined next.

The effect of particle–turbulence interactions on the spectral components of near-field pressure are shown in figure 14. With increasing Mach number, the spectrum broadens due to the Mach wave radiation mechanism (Laufer, Schlinker & Kaplan 1976); Mach-like waves are indeed apparent in visualizations provided in figure 12(*c*–*f*). The universal decrease observed in the mid-plane pressure spectra with the addition of particles (see figure 8) does not hold for the pressure outside of the turbulence, suggesting that a source-to-sound decomposition is not straightforward for $M \lesssim 1.5$. The subsonic case shows an increase in spectral components and slight spectral broadening while $M = 2.5$ shows the opposite effect which has implications for perceived sound levels. The perceived sound field changes from $M = 2.5$ might be significant if the Mach wave radiation is reduced, as evidenced by the reduction of E_p for wavenumbers $5 \lesssim k_x\delta_m \lesssim 40$.

To quantify the changes in sound pressure levels, figure 15(*a*) shows the decibel difference, based on average pressure intensity, with respect to the unladen ($\Phi_m = 0$) cases as defined by

$$\Delta\mathrm{SPL}(y, t) = 10 \log_{10}\left(\frac{\overline{p'p'}(y, t, \Phi_m)}{\overline{p'p'}(y, t, \Phi_m = 0)}\right), \tag{4.1}$$

taken at $y = 20\delta_m$. A similar quantity for the degree of sound reduction in jet turbulence has been used previously (Papamoschou 2000). For (4.1), negative values of ΔSPL indicate sound level reduction relative to the baseline. The sound field

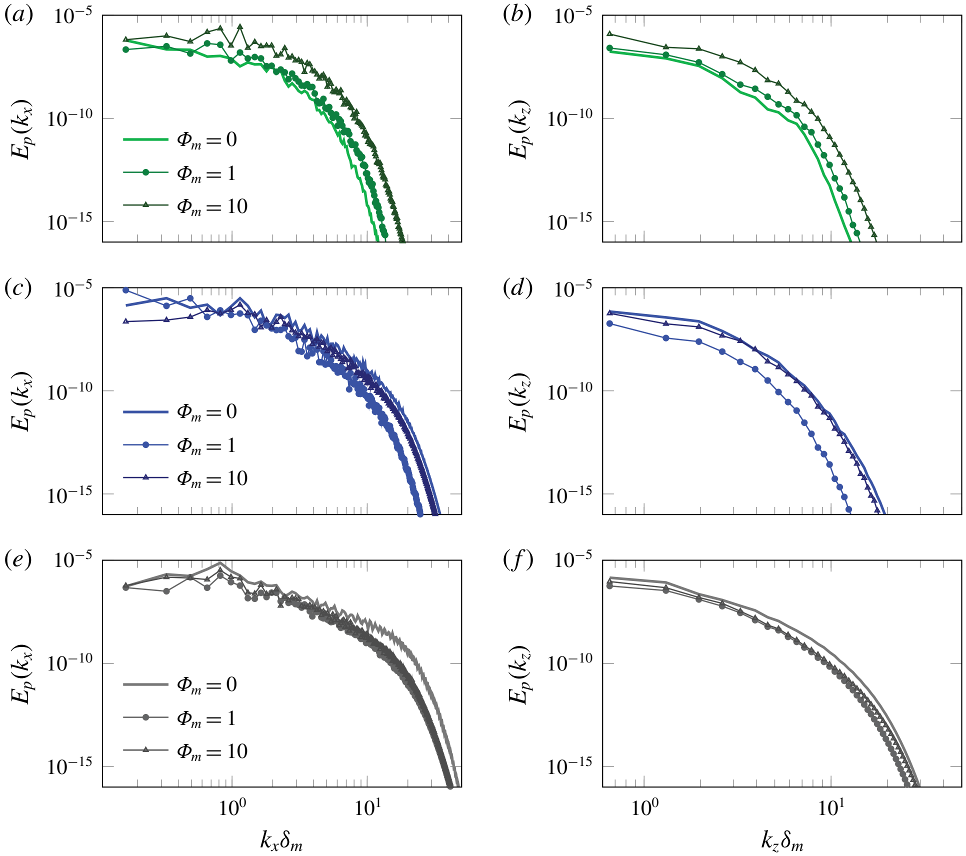

FIGURE 14. (Colour online) (*a*,*c*,*e*) Streamwise and (*b*,*d*,*f*) spanwise pressure spectra, respectively, at $y = 20\delta_m$ when $\delta_m/\delta_m^o = 20$: (*a*,*b*) $M = 0.9$, (*c*,*d*) $M = 1.5$ and (*e*,*f*) $M = 2.5$. All spectral components are normalized by $\Delta U^4 \rho_\infty^2 \delta_m$.

changes in figure 15(*a*) are observed to have Mach number and mass loading dependence. For Mach numbers $M \gtrsim 1.5$, sound reduction is observed for $\Phi_m \gtrsim 1$, which is consistent with previous experimental observations (Krothapalli *et al.* 2003; Greska 2005). Contrasting this, subsonic flows show a sound level increase with mass loading, by as much as ≈6 dB. These observations occur despite universal decrease in the mid-plane average turbulent kinetic energy as quantified in figure 15(*b*). In the following section, possible mechanisms for the observed sound changes, especially the sound level increase for $M = 0.9$, are considered.

4.4. *A pithy discussion of* ΔSPL *and low-speed aeroacoustics theory*

Crighton & Ffowcs Williams (1969) provided a theoretical prediction for sound changes in two-phase turbulence using Lighthill's acoustic analogy framework. Instead of sound reduction, which was later observed in high-speed jets (Krothapalli *et al.* 2003), their theory predicted enhancement of sound radiation: up to 70 dB increase for air bubbles in water and up to 20 dB increase for solid particles in air. Based on their theory, the largest sound modification was linked to increasing the mixture

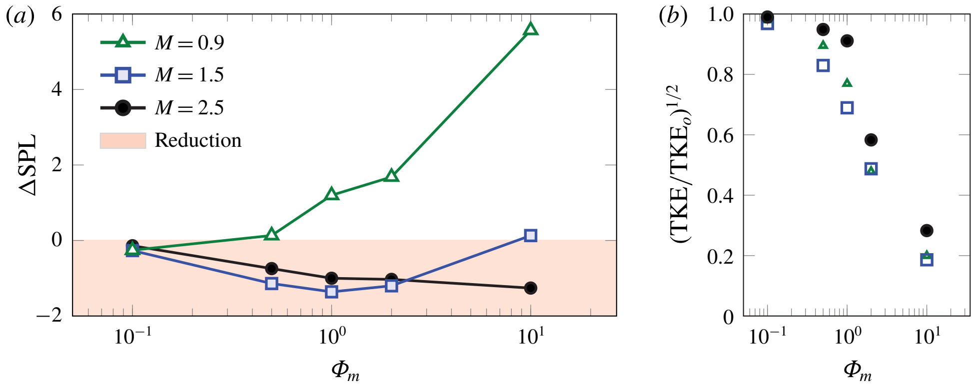

FIGURE 15. (Colour online) (*a*) Sound pressure level change at $y/\delta_m = 20$ and (*b*) reduction in turbulence level at $y/\delta_m = 0$. All data are presented for $St = 1$.

density by the mass fraction

$$\rho_m = \rho(1 + \Phi_m), \tag{4.2}$$

which affects the speed of sound ratio between the disperse-phase–fluid mixture (c_m) and the fluid phase (c_∞)

$$\left(\frac{c_m}{c_\infty}\right)^2 = \frac{1}{(1 + \Phi_m)}. \tag{4.3}$$

Without presenting the full details of the formulation, which is a consequence of the governing equations (i.e. mass and momentum conservation), the acoustic efficiency is

$$\eta = \frac{\mathcal{I}}{\rho U^4 L^2} \sim \frac{1}{4\pi}(\mathrm{TKE}^{1/2} M)^5 \left(\frac{c_\infty}{c_m}\right)^c \left(\frac{L}{l_o}\right), \tag{4.4}$$

with $\mathcal{I}$ the acoustic intensity, $U = \Delta U$ for shear layers, L the large-scale length, l_o the turbulence length scale and the power c of the speed of sound ratio depends on the mass loading. The efficiency increases from the sound-speed ratio depending on the mass loading with power $c = 6$ for $\Phi_m > 1$ and $c = 2$ for $\Phi_m < 1$ (Crighton & Ffowcs Williams 1969). It also scales with M^5, consistent with the expected behaviour for single-phase flow (Lighthill 1952). For large mass loadings $\Phi_m > 1$, the acoustic intensity is $\mathcal{I} \propto (c_\infty/c_m)^8$ using (4.3), which assumes that the scales of turbulence (intensity and length) and mean driving velocity (U) are independent of mass loading. Figure 16 shows that the theory overpredicts ΔSPL compared to the $M = 0.9$ shear-flow turbulence, which was chosen as a candidate to compare with the low-speed theory. Although there are relatively modest changes to the mean flow $\overline{u}(y)$ and energetic scales (see § 4), the particle-laden flow turbulence intensity decreases with Φ_m, shown in figure 15(*b*), which is one cause for discrepancy with the theory. Including the relative turbulence intensity effect and using ΔSPL in (4.1) yields a modified estimate

$$\Delta\mathrm{SPL} \sim 10\log_{10}\left[(1 + \Phi_m)^a \left(\frac{\mathrm{TKE}}{\mathrm{TKE}_o}\right)^{b/2}\right], \tag{4.5}$$

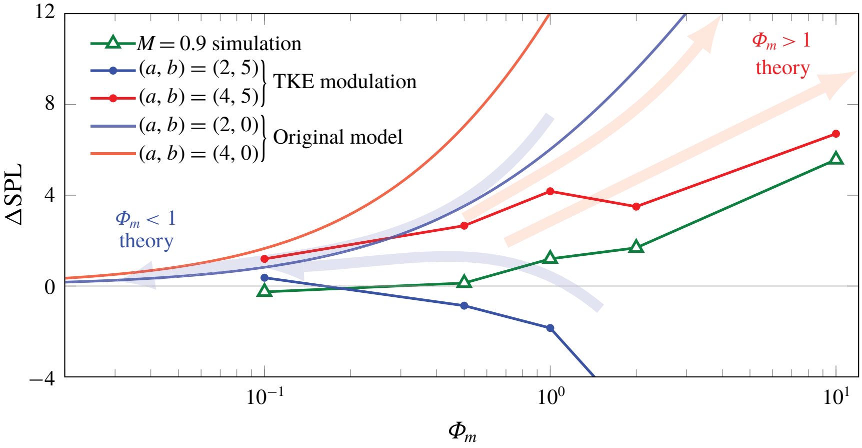

FIGURE 16. (Colour online) Models of low-speed sound modulation compared to the $M = 0.9$ case: $\Phi_m \gtrsim 1$ models in red and $\Phi_m \lesssim 1$ models in blue. Factors a (Φ_m effect) and b (TKE effect) apply to equation (4.5): original model neglected TKE modulation ($b = 0$).

where $(a, b) = (4, 5)$ for $\Phi_m > 1$ and $(a, b) = (2, 5)$ for $\Phi_m < 1$, respectively. This modification trends closer to the $M = 0.9$ simulation in figure 16. Note that setting $b = 0$ in (4.5) yields the original expectation of Crighton & Ffowcs Williams (1969) for which turbulence intensity is assumed Φ_m-independent. For $\Phi_m < 1$, the increase in sound is much less significant following $\mathcal{I} \propto (1 + \Phi_m)^2$ and the effect of turbulence modification small since $\mathrm{TKE}/\mathrm{TKE}_o \approx 1$ for very small mass loadings ($\Phi_m < 0.1$), which is consistent with expectation and simulations for which $\Phi_m \ll 1$ has little effect on the sound. Improvements can still be made since the Crighton & Ffowcs Williams (1969) theory omits turbulence convection effects and assumes sources are acoustically compact. Although this is a reasonable approximation for $M \ll 1$, at high-speed, turbulence convection affects acoustic efficiency (Ffowcs Williams 1963). Furthermore, the theory also assumes that the particles exactly follow the flow (i.e. $\boldsymbol{u}_p = \boldsymbol{u}_f$) and that the volume displacement due to particles is small. Based on the local pressure intensity budget in figure 11(*c*,*f*,*i*), volume displacement effects and drag coupling due to local slip velocity $|\boldsymbol{u}_p - \boldsymbol{u}_f| > 0$ are sizable sources and sinks. Although, their combined causal effect in retarded time on the radiated acoustic intensity remains to be seen. In the current framework, a flow closer to what Crighton & Ffowcs Williams (1969) envisioned, for $M \ll 1$, could be designed by reducing the particle diameter so that $\Phi_v \ll 1$ and $St \ll 1$. However, the computational cost to maintain $0.1 < \Phi_m < 10$, reducing d_p, would be significant and outside the scope of the paper for which finite-sized, inertial particles, based on water droplets, in high-speed turbulence are of interest. Thus, a direct comparison to the Crighton & Ffowcs Williams (1969) theory was not made beyond this, nor for situations extending beyond the low-speed theory. In a $M \gg 1$ limit, there are additional important effects (e.g. non-compactness of acoustic sources).

As discussed, particles in high-speed shear flows can affect the sound radiation by sound-speed effects (c_m due to Φ_m) and due to turbulence changes. For micro-jet injection into round jets, data show that the sound-speed effect is weak; that is, sound radiation for micro-jet gas injection (with gas sound speed approximately equal to the jet) is similar to that of liquid micro-droplet injection (Greska 2005), which supports a primary hydrodynamic effect for sound changes. Likewise, in the current simulations, which do not account for speed of sound effects, *viz.*, a mixture equation of state in (4.3), the changes in sound intensity are due to changes in the nature of the turbulence and to additional sound sources from particle interactions.

For subsonic flows, sound changes can come from subtle modifications to the turbulence; the time rate of change of the eddies leads to sound radiation (e.g. Crighton 1975). Thus, the turbulence sources, based on its dilatation and rate of changes, are shown in figure 17 since they can provide sources of sound (Ribner 1962; Ristorcelli 1997). In the turbulence, the rate of dilatation changes in the $M=0.9$ case in figure 17(*b*) increases, by over an order of magnitude in the domain, due to the presence of particles, which can provide a source to its increased radiated $\overline{p'p'}$ beyond $y \gtrsim 5\ \delta_m$. For $M = 2.5$ in figure 17(*f*), these rates of change are already large for $\Phi_m = 0$ so the effect of particles, beyond that of the baseline turbulence, is relatively small. The $M = 2.5$ sound changes can be linked to the domain-wide decrease in dilatation (and turbulence decrease), shown in figure 17(*e*), which concurs with its decrease in sound intensity. Similar observations for dilatation were made from particle-laden supersonic convecting spatially developing turbulence simulations for $\Phi_m = 0.5$ (Dai *et al.* 2018).

5. Conclusions and discussion

Numerical simulations of particle-laden high-speed planar shear-flow turbulence are used to examine the particle–turbulence coupling effects on velocity and pressure fluctuations. Interphase coupling has a broadband effect on the turbulence and pressure fields – reducing the turbulence by over 70 % for mass loading $\Phi_m = 10$. Analysis of pressure intensity transport mechanisms show that changes in the intensity follow primarily from changes to the turbulence. Local pressure intensity sources and sinks from volume displacement and drag coupling, respectively, are only substantial for $\Phi_m \gtrsim 1$. For subsonic shear layers ($M = 0.9$), these two effects approximately cancel, obfuscating possible mechanisms for their near-field sound changes; however, significant changes to fluid dilatation rates (with Φ_m) indicate a potential mechanism for increasing net sound radiation for $\Phi_m \gtrsim 1$. These results motivate alternative descriptions of sound-reducing mechanisms and source-to-sound decompositions for guiding design, especially for more complex configurations. For example, simplified turbulence source descriptions (e.g. wave packets) may facilitate analysis for the growing–decaying turbulence dynamics which underpin sound radiation in subsonic single-phase flow (Jordan & Colonius 2013). Contrasting lower-speed particle-laden flow turbulence simulations, sound radiation decreases with $0.1 \lesssim \Phi_m \lesssim 10$ for supersonic convection shear layers ($M > 1.5$) as well as a decrease in turbulence and dilatation levels. Modest sound reductions, $\lesssim$2 dB for $M = 2.5$ concur with observations that sound radiation in supersonic flows is relatively insensitive to source changes, for example, due to its turbulence structure (Buchta & Freund 2019).

Acknowledgements

The authors thank R. Vishnampet for access to his single-phase compressible flow solver and J. Kim for his detailed comments on an earlier draft of the manuscript. A portion of the single-phase simulation framework was developed by D. A. Buchta while a student of Professor Freund at the University of Illinois. This research used resources of the Oak Ridge Leadership Computing Facility at the Oak Ridge National Laboratory, which is supported by the Office of Science of the U.S. Department of

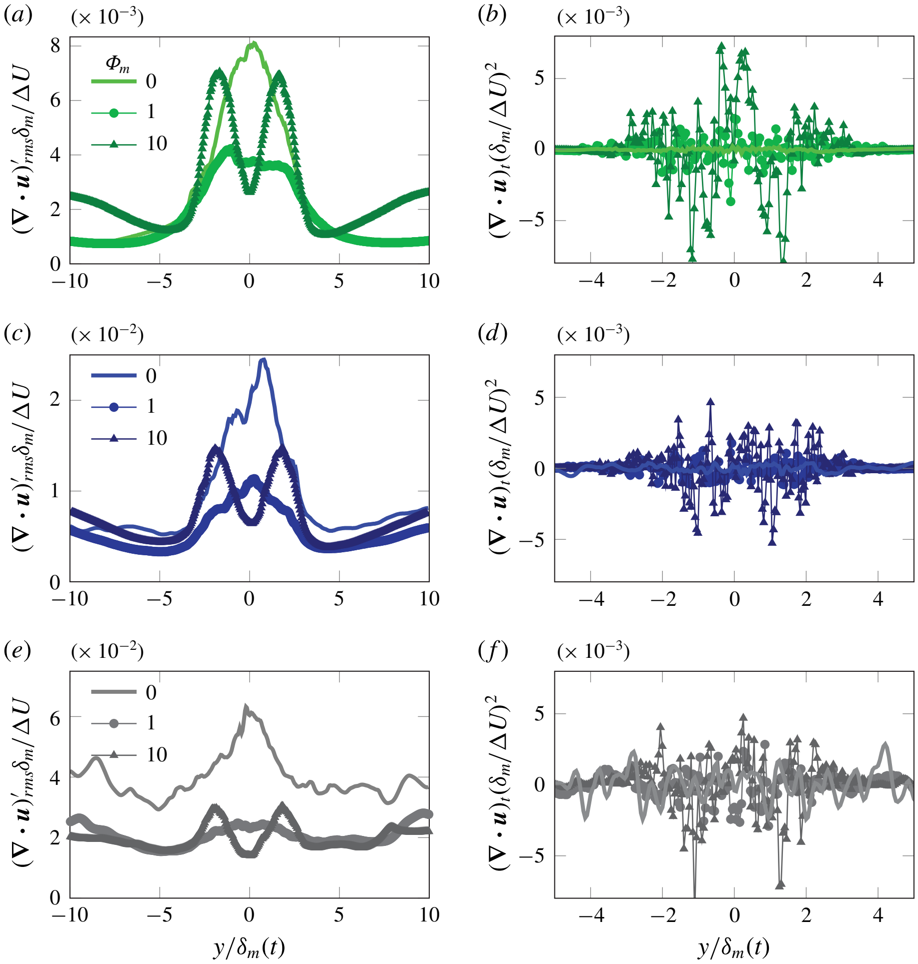

FIGURE 17. (Colour online) (*a*,*c*,*e*) Average fluctuating dilatation and (*b*,*d*,*f*) average instantaneous rate of change of dilatation when $\delta_m/\delta_m^o = 20$: (*a*,*b*) $M = 0.9$, (*c*,*d*) $M = 1.5$ and (*e*,*f*) $M = 2.5$.

Energy under contract no. DE-AC05-00OR22725 through the Director's Discretionary Program and from the Advanced Research Computing Technology Services at the University of Michigan. Part of this work was supported by a NASA Space Technology Research Fellowship.

Appendix A. Volume filtering the compressible flow equations

This section provides the volume-filtered derivation of the viscous compressible Navier–Stokes equations used in the simulations. Attention is paid to the energy equation as the majority of work to this date has focused on incompressible flows. Here we extend the local averaging procedure of Anderson & Jackson (1967) to the compressible Navier–Stokes equations,

$$\frac{\partial \rho^*}{\partial t} + \nabla\cdot(\rho^*\boldsymbol{u}^*) = 0, \tag{A 1}$$

$$\frac{\partial \rho^* \boldsymbol{u}^*}{\partial t} + \boldsymbol{\nabla} \boldsymbol{\cdot} (\rho^* \boldsymbol{u}^* \otimes \boldsymbol{u}^* + p^* \mathbb{I} - \boldsymbol{\tau}^*) = 0, \tag{A 2}$$

and

$$\frac{\partial \rho^* E^*}{\partial t} + \boldsymbol{\nabla} \boldsymbol{\cdot} (\{\rho^* E^* + p^*\} \boldsymbol{u}^* + \boldsymbol{q}^* - \boldsymbol{u}^* \boldsymbol{\cdot} \boldsymbol{\tau}^*) = 0, \tag{A 3}$$

where superscript $*$ indicates a microscale quantity (i.e. a scalar or vector field resolved at the scale of an individual particle), and $\mathbb{I}$ is the identity matrix. The relation between microscale pressure and total energy is

$$p^* = (\gamma - 1) \left(\rho^* E^* - \tfrac{1}{2} \rho^* \boldsymbol{u}^* \boldsymbol{\cdot} \boldsymbol{u}^*\right). \tag{A 4}$$

Finally, the ideal gas law (in non-dimensional form) is given by

$$T^* = \frac{\gamma p^*}{\rho^* (\gamma - 1)}. \tag{A 5}$$

In order to account for the effect of particles without requiring to resolve the fluid-phase equations on the scale of the particle surface, the Navier–Stokes equations are split into microscale (particle-scale) processes, and mesoscale processes, i.e. processes that take place on a scale much larger than the particle diameter. To facilitate a description of this length-scale separation, a filtering kernel $\mathcal{G}$ is used with a characteristic length δ_f, such that $\mathcal{G}(r) > 0$ decreases monotonically with increasing r, and is normalized such that its integral over the entire physical space is unity. The local voidage at a point $\boldsymbol{x}$ and time t is defined as

$$\alpha(\boldsymbol{x}, t) = \int_{\mathcal{V}_f} \mathcal{G}(|\boldsymbol{x} - \boldsymbol{y}|) \, \mathrm{d}\boldsymbol{y}, \tag{A 6}$$

where $\mathcal{V}_f$ indicates that the integral is taken over all points $\boldsymbol{y}$ occupied by the fluid. Due to contributions at the particle surface, there is no commutation between filtering and differentiation. Consequently, filtering derivatives of point variables will lead to additional terms in the form of integrals of the pointwise quantity about the surface of the particle. Volume filtering the gradient, divergence and time derivative of a point property of the fluid $\boldsymbol{a}^*$ are respectively given as

$$\int_{\mathcal{V}_f} \boldsymbol{\nabla} \boldsymbol{a}^*(\boldsymbol{y}, t) \mathcal{G}(|\boldsymbol{x} - \boldsymbol{y}|) \, \mathrm{d}\boldsymbol{y} = \boldsymbol{\nabla} (\alpha \boldsymbol{a}(\boldsymbol{x}, t)) - \sum_{i=1}^{N_p} \int_{\mathcal{S}_i} \boldsymbol{n} \otimes \boldsymbol{a}^*(\boldsymbol{y}, t) \mathcal{G}(|\boldsymbol{x} - \boldsymbol{y}|) \, \mathrm{d}\boldsymbol{y}, \tag{A 7}$$

$$\int_{\mathcal{V}_f} \boldsymbol{\nabla} \boldsymbol{\cdot} \boldsymbol{a}^*(\boldsymbol{y}, t) \mathcal{G}(|\boldsymbol{x} - \boldsymbol{y}|) \, \mathrm{d}\boldsymbol{y} = \boldsymbol{\nabla} \boldsymbol{\cdot} (\alpha \boldsymbol{a}(\boldsymbol{x}, t)) - \sum_{i=1}^{N_p} \int_{\mathcal{S}_i} \boldsymbol{n} \boldsymbol{\cdot} \boldsymbol{a}^*(\boldsymbol{y}, t) \mathcal{G}(|\boldsymbol{x} - \boldsymbol{y}|) \, \mathrm{d}\boldsymbol{y}, \tag{A 8}$$

and

$$\int_{\mathcal{V}_f} \frac{\partial \boldsymbol{a}^*(\boldsymbol{y}, t)}{\partial t} \mathcal{G}(|\boldsymbol{x} - \boldsymbol{y}|) \, \mathrm{d}\boldsymbol{y} = \frac{\partial}{\partial t} (\alpha \boldsymbol{a}(\boldsymbol{x}, t)) + \sum_{i=1}^{N_p} \int_{\mathcal{S}_i} \boldsymbol{n} \boldsymbol{\cdot} \boldsymbol{v}_p^{(i)} \boldsymbol{a}^*(\boldsymbol{y}, t) \mathcal{G}(|\boldsymbol{x} - \boldsymbol{y}|) \, \mathrm{d}\boldsymbol{y}, \tag{A 9}$$

where $\mathcal{S}_i$ represents the surface of particle i, $\boldsymbol{n}$ is the unit normal vector outward from the surface of the particle and $\boldsymbol{v}_p^{(i)}$ is its velocity.

Applying these definitions to the microscale density equation (A 1) yields

$$\frac{\partial \alpha\rho}{\partial t} + \nabla\boldsymbol{\cdot}(\alpha\rho\boldsymbol{u}) = 0. \tag{A 10}$$

Volume filtering the pressure gradient term in the momentum equation yields

$$\int_{\mathcal{V}_f} \nabla p^* \mathcal{G}(|\boldsymbol{x}-\boldsymbol{y}|)\,\mathrm{d}\boldsymbol{y} = \nabla(\alpha p) - \sum_{i=1}^{N_p}\int_{\mathcal{S}_i} \boldsymbol{n}p^*\mathcal{G}(|\boldsymbol{x}-\boldsymbol{y}|)\,\mathrm{d}\boldsymbol{y}, \tag{A 11}$$

where $\boldsymbol{n}p^*$ represents the interfacial pressure. Decomposing the local pressure $p^* = p + p'$, the second term on the right-hand side can be expressed as

$$\sum_{i=1}^{N_p}\int_{\mathcal{S}_i} \boldsymbol{n}p^*\mathcal{G}(|\boldsymbol{x}-\boldsymbol{y}|)\,\mathrm{d}\boldsymbol{y} = \sum_{i=1}^{N_p}\int_{\mathcal{S}_i} \boldsymbol{n}p\mathcal{G}(|\boldsymbol{x}-\boldsymbol{y}|)\,\mathrm{d}\boldsymbol{y} + \sum_{i=1}^{N_p}\int_{\mathcal{S}_i} \boldsymbol{n}p'\mathcal{G}(|\boldsymbol{x}-\boldsymbol{y}|)\,\mathrm{d}\boldsymbol{y}, \tag{A 12}$$

where the last term involving surface contributions of the sub-filtered pressure p' is unclosed. Assuming the characteristic size of the filter kernel $\delta_f \gg d_p$, p varies little over the surface of the particle and can be taken out of the integral of the first term on the right-hand side. Applying the divergence theorem, the volume-filtered pressure gradient can be expressed as

$$\int_{\mathcal{V}_f} \nabla p^* \mathcal{G}(|\boldsymbol{x}-\boldsymbol{y}|)\,\mathrm{d}\boldsymbol{y} = \nabla(\alpha p) - p\nabla\alpha - \sum_{i=1}^{N_p}\int_{\mathcal{S}_i} \boldsymbol{n}p'\mathcal{G}(|\boldsymbol{x}-\boldsymbol{y}|)\,\mathrm{d}\boldsymbol{y}, \tag{A 13}$$

where the last term on the right-hand side of (A 13) needs to be modelled. Here, $p\nabla\alpha$ represents a nozzling term that accelerates the gas due to particles restricting the area where fluid can flow (Houim & Oran 2016). Applying the same procedure to the viscous stress tensor, the volume-filtered momentum equation can be expressed as

$$\frac{\partial \alpha\rho\boldsymbol{u}}{\partial t} + \nabla\boldsymbol{\cdot}(\alpha\{\rho\boldsymbol{u}\otimes\boldsymbol{u} + p\mathbb{I} - \boldsymbol{\tau} + \boldsymbol{R}\}) = (p\mathbb{I} - \boldsymbol{\tau})\boldsymbol{\cdot}\nabla\alpha + \boldsymbol{F}, \tag{A 14}$$

where $\boldsymbol{R}$ is akin to a Reynolds stress in the context of large-eddy simulations (referred to as the pseudo-turbulent Reynolds stress (Mehrabadi *et al.* 2015)) and contains sub-filtered velocity fluctuations due to, for example, wakes past particles; $\boldsymbol{F}$ represents a sub-filtered momentum exchange term that is typically modelled using drag correlations based on local Reynolds number, Mach number and volume fraction (Clift *et al.* 2005). In low Mach number flows, it is common to simplify the momentum equation by employing the product rule, i.e. $\nabla(\alpha p) = p\nabla\alpha + \alpha\nabla p$, such that the non-conservative nozzling term ($p\nabla\alpha$) cancels with the first term on the right-hand side of equation (A 14) (Capecelatro & Desjardins 2013). Therefore, under the assumption of an incompressible disperse phase, and neglecting $\boldsymbol{R}$ as is typically done in simulations of fluid–particle flows, the momentum equation can be expressed as

$$\frac{\partial \alpha\rho\boldsymbol{u}}{\partial t} + \nabla\boldsymbol{\cdot}(\alpha\rho\boldsymbol{u}\otimes\boldsymbol{u}) + \alpha\nabla\boldsymbol{\cdot}(p\mathbb{I} - \boldsymbol{\tau}) = \boldsymbol{F}. \tag{A 15}$$

For the gas-phase energy equation (A 3), volume filtering the work done by pressure yields

$$\int_{\mathcal{V}_f} \nabla \cdot (p^* \boldsymbol{u}^*) \mathcal{G}(|\boldsymbol{x}-\boldsymbol{y}|)\, \mathrm{d}\boldsymbol{y} = \nabla \cdot (\alpha p \boldsymbol{u}) - \sum_{i=1}^{N_p} \int_{\mathcal{S}_i} \boldsymbol{n} \cdot (p^* \boldsymbol{u}^*) \mathcal{G}(|\boldsymbol{x}-\boldsymbol{y}|)\, \mathrm{d}\boldsymbol{y}. \quad \text{(A 16)}$$

The fluid-phase velocity at the surface of the particle can be decomposed into $\boldsymbol{u}^*|_{\mathcal{S}_i} = \boldsymbol{v}_p^{(i)} + \dot{r}_p^{(i)} \boldsymbol{n}$, where $\dot{r}_p^{(i)}$ is the rate of change of the radius of particle i. Decomposing the pressure into its filtered and sub-filtered contributions, and assuming rigid particles (i.e. $\dot{r}_p = 0$), the last term on the right-hand side of (A 16) becomes

$$\begin{aligned} &\sum_{i=1}^{N_p} \int_{\mathcal{S}_i} \boldsymbol{n} \cdot (p^* \boldsymbol{u}^*) \mathcal{G}(|\boldsymbol{x}-\boldsymbol{y}|)\, \mathrm{d}\boldsymbol{y} \\ &\quad = p \sum_{i=1}^{N_p} \int_{\mathcal{S}_i} \boldsymbol{n} \cdot \boldsymbol{v}_p^{(i)} \mathcal{G}(|\boldsymbol{x}-\boldsymbol{y}|)\, \mathrm{d}\boldsymbol{y} + \sum_{i=1}^{N_p} \int_{\mathcal{S}_i} p' \boldsymbol{n} \cdot \boldsymbol{v}_p^{(i)} \mathcal{G}(|\boldsymbol{x}-\boldsymbol{y}|)\, \mathrm{d}\boldsymbol{y}. \end{aligned} \quad \text{(A 17)}$$

Applying (A 9) to the first term on the right-hand side of (A 17) with $\boldsymbol{a}^* = 1$ yields

$$\int_{\mathcal{V}_f} \nabla \cdot (p^* \boldsymbol{u}^*) \mathcal{G}(|\boldsymbol{x}-\boldsymbol{y}|)\, \mathrm{d}\boldsymbol{y} = \nabla \cdot (\alpha p \boldsymbol{u}) + p \frac{\partial \alpha}{\partial t} - \sum_{i=1}^{N_p} \int_{\mathcal{S}_i} p' \boldsymbol{n} \cdot \boldsymbol{v}_p^{(i)} \mathcal{G}(|\boldsymbol{x}-\boldsymbol{y}|)\, \mathrm{d}\boldsymbol{y}, \quad \text{(A 18)}$$

where $p\partial\alpha/\partial t$ represents a pDV work term due to particles entering and leaving a control volume (Lhuillier *et al.* 2010). Because $\boldsymbol{v}_p$ is constant over the surface of the particle, it can be brought outside of the integral in the last term on the right-hand side of equation (A 18), resulting in $\sum_{i=1}^{N_p} \boldsymbol{v}_p^{(i)} \cdot \int_{\mathcal{S}_i} p' \boldsymbol{n} \mathcal{G}(|\boldsymbol{x}-\boldsymbol{y}|)\, \mathrm{d}\boldsymbol{y}$. This sub-filtered term is now identical to the closure appearing in the momentum equation (A 12) (but multiplied by the particle velocity). As described by Ling, Balachandar & Parmar (2016), multiplying $\boldsymbol{F}$ by the particle velocity ensures the microscale kinetic energy is dissipated and transferred to the internal energy of the fluid. Using a similar procedure for the viscous stress tensor, the volume-filtered energy equation can be expressed as

$$\frac{\partial \alpha \rho E}{\partial t} + \nabla \cdot \alpha (\{\rho E + p\} \boldsymbol{u} - \boldsymbol{u} \cdot \boldsymbol{\tau}) + \alpha \nabla \cdot \boldsymbol{q} = -p \frac{\partial \alpha}{\partial t} + \boldsymbol{\tau} : \nabla (\alpha_p \boldsymbol{u}_p) + \boldsymbol{u}_p \cdot \boldsymbol{F} + Q, \quad \text{(A 19)}$$

where Q is a sub-filtered heat exchange term that can be modelled using Nusselt number correlations based on local Reynolds number and volume fraction (Gunn 1978; Tenneti *et al.* 2013), and $\boldsymbol{u}_p$ is an Eulerian representation of the particle-phase velocity. Here we neglect sub-filter terms that involve correlations between particle-scale velocity, temperature and viscous stresses. The Eulerian particle-phase velocity $\boldsymbol{u}_p$ can be obtained via

$$\alpha_p \boldsymbol{u}_p = \sum_{i=1}^{N_p} \boldsymbol{v}_p^{(i)} \mathcal{G}(|\boldsymbol{x} - \boldsymbol{x}_p^{(i)}|) V_p, \quad \text{(A 20)}$$

where V_p is the particle volume. Houim & Oran (2016) replaced the pDV work term by employing the disperse-phase continuity equation assuming constant particle density, i.e.

$$p \frac{\partial \alpha}{\partial t} = -p \frac{\partial \alpha_p}{\partial t} = p \nabla \cdot (\alpha_p \boldsymbol{u}_p). \quad \text{(A 21)}$$

Expressing this source term in terms of volume fraction gradients as opposed to the rate of change of volume fraction facilitates its solution.

Filtering the equation of state (A 4) is now considered by applying the following decomposition to microscale quantities

$$p+p' = (\gamma-1)\{\rho E + \rho E' - \tfrac{1}{2}(\rho+\rho')(u_i+u_i'')(u_i+u_i'')\}, \tag{A 22}$$

which also invokes decomposition $u^* = u + u''$, indicating a density-weighted (Favre) filter for the velocity components. Volume filtering (A 22) yields

$$\begin{aligned}\alpha p = (\gamma-1)\Bigg\{&\alpha\rho E - \alpha\frac{1}{2}\rho u_i u_i \\ &- \frac{1}{2}\int_{\mathcal{V}_f}[2\rho u_i u_i'' + 2u_i\rho' u_i'' + \rho' u_i u_i + \rho u_i'' u_i'' + \rho' u_i'' u_i'']\mathcal{G}(|\boldsymbol{x}-\boldsymbol{y}|)\,\mathrm{d}\boldsymbol{y}\Bigg\},\end{aligned} \tag{A 23}$$

which simplifies to

$$p = (\gamma-1)(\rho E - \tfrac{1}{2}\rho\boldsymbol{u}\boldsymbol{\cdot}\boldsymbol{u} - \tfrac{1}{2}R_{ii}). \tag{A 24}$$

Neglecting the sub-filtered mechanisms contained in R_{ii}, as done in (A 15), yields the volume-filtered equation of state in equation (2.6). Finally, a similar decomposition is applied to the ideal gas law (A 5),

$$p+p' = \frac{\gamma-1}{\gamma}(\rho+\rho')(T+T''), \tag{A 25}$$

where Favre decomposition is used for temperature. Volume filtering (A 25) and using the definition of a Favre filter yields the closed-form gas law (equation (2.7) in § 2)

$$T = \frac{\gamma p}{\rho(\gamma-1)}. \tag{A 26}$$

REFERENCES

AGRAWAL, K., HOLLOWAY, W., MILIOLI, C. C., MILIOLI, F. E. & SUNDARESAN, S. 2013 Filtered models for scalar transport in gas–particle flows. *Chem. Engng Sci.* **95**, 291–300.

AGRAWAL, K., LOEZOS, P. N., SYAMLAL, M. & SUNDARESAN, S. 2001 The role of meso-scale structures in rapid gas-solid flows. *J. Fluid Mech.* **445**, 151–185.

ALKISLAR, M. B. & BUTLER, G. W. 2007 Significant improvements on jet noise reduction by chevron–microjet combination. *AIAA Paper* 2007-3598, pp. 21–23.

ANDERSON, T. B. & JACKSON, R. 1967 Fluid mechanical description of fluidized beds. Equations of motion. *Ind. Engng Chem. Fundam.* **6** (4), 527–539.

BALACHANDAR, S. & EATON, J. K. 2010 Turbulent dispersed multiphase flow. *Annu. Rev. Fluid Mech.* **42**, 111–133.

BATTISTA, F., GUALTIERI, P., MOLLICONE, J. P. & CASCIOLA, C. M. 2018 Application of the exact regularized point particle method (ERPP) to particle laden turbulent shear flows in the two-way coupling regime. *Intl J. Multiphase Flow* **101**, 113–124.

BOWES, W., RUMPF, D., BOWLER, D., CARNES, R., FRATARANGELO, P., HEISER, W. H., HU, D. L., MOIN, P. & VOORHEES, W. J. 2009 Report on jet engine noise reduction. *Tech. Rep.* Naval Research Advisory Committee.

BRILEY, W. R. & MCDONALD, H. 1977 Solution of the multidimensional compressible Navier–Stokes equations by a generalized implicit method. *J. Comput. Phys.* **24** (4), 372–397.

BUCHTA, D. A. 2016 Crackle noise from high-speed free-shear-flow turbulence. PhD thesis, University of Illinois at Urbana–Champaign.

BUCHTA, D. A. & FREUND, J. B. 2017 The near-field pressure radiated by planar high-speed free-shear-flow turbulence. *J. Fluid Mech.* **832**, 383–408.

BUCHTA, D. A. & FREUND, J. B. 2019 Intense sound radiation by high-speed flow: turbulence structure, gas properties, and near-field gas dynamics. *Phys. Rev. Fluids* **4**, 044605.

CAPECELATRO, J. & BUCHTA, D. 2017 Direct numerical simulation of noise suppression by water injection in high-speed flows. In *55th AIAA Aerospace Sciences Meeting*. AIAA.

CAPECELATRO, J. & DESJARDINS, O. 2013 An Euler–Lagrange strategy for simulating particle-laden flows. *J. Comput. Phys.* **238**, 1–31.

CAPECELATRO, J., DESJARDINS, O. & FOX, R. O. 2015 On fluid-particle dynamics in fully developed cluster-induced turbulence. *J. Fluid Mech.* **780**, 578–635.

CAPECELATRO, J., DESJARDINS, O. & FOX, R. O. 2018 On the transition between turbulence regimes in particle-laden channel flows. *J. Fluid Mech.* **845**, 499–519.

CLECKLER, J., ELGHOBASHI, S. & LIU, F. 2012 On the motion of inertial particles by sound waves. *Phys. Fluids* **24** (3), 033301.

CLIFT, R., GRACE, J. R. & WEBER, M. E. 2005 *Bubbles, Drops, and Particles*. Courier Corporation.

CRIGHTON, D. G. 1975 Basic principles of aerodynamic noise generation. *Prog. Aerosp. Sci.* **16** (1), 31–96.

CRIGHTON, D. G. & FFOWCS WILLIAMS, J. E. 1969 Sound generation by turbulent two-phase flow. *J. Fluid Mech.* **36** (3), 585–603.

DAI, Q., JIN, T., LUO, K. & FAN, J. 2018 Direct numerical simulation of particle dispersion in a three-dimensional spatially developing compressible mixing layer. *Phys. Fluids* **30** (11), 113302.

DEBISSCHOP, J. R., CHAMBRES, O. & BONNET, J. P. 1994 Velocity field characteristics in supersonic mixing layers. *Exp. Therm. Fluid Sci.* **9** (2), 147–155.

EATON, J. K. & FESSLER, J. R. 1994 Preferential concentration of particles by turbulence. *Intl J. Multiphase Flow* **20**, 169–209.

ELGHOBASHI, S. & TRUESDELL, G. C. 1993 On the two-way interaction between homogeneous turbulence and dispersed solid particles. I. Turbulence modification. *Phys. Fluids* A **5** (7), 1790–1801.

ELLIOTT, G. S. & SAMIMY, M. 1990 Compressibility effects in free shear layers. *Phys. Fluids* A **2** (7), 1231–1240.

FFOWCS WILLIAMS, J. E. 1963 The noise from turbulence convected at high speed. *Phil. Trans. R. Soc. Lond.* A **255** (1061), 469–503.

FFOWCS WILLIAMS, J. E. & MAIDANIK, G. 1965 The Mach wave field radiated by supersonic turbulent shear flows. *J. Fluid Mech.* **21**, 641–657.

FOX, R. O. 2014 On multiphase turbulence models for collisional fluid–particle flows. *J. Fluid Mech.* **742**, 368–424.

FREUND, J. B. 1997 Proposed inflow/outflow boundary condition for direct computation of aerodynamic sound. *AIAA J.* **35** (4), 740–742.

GILINSKY, M., BHAT, T. & SEINER, J. 1994 Supersonic gasdispersional jets – models and applications. In *32nd Aerospace Sciences Meeting and Exhibit*. AIAA.

GLASSER, B. J., SUNDARESAN, S. & KEVREKIDIS, I. G. 1998 From bubbles to clusters in fluidized beds. *Phys. Rev. Lett.* **81**, 1849–1852.

GOEBEL, S. G. & DUTTON, J. C. 1991 Experimental study of compressible turbulent mixing layers. *AIAA J.* **29** (4), 538–546.

GRESKA, B. J. 2005 Supersonic jet noise and its reduction using microjet injection. PhD thesis, Florida State University.

GUALTIERI, P., BATTISTA, F. & CASCIOLA, C. M. 2017 Turbulence modulation in heavy-loaded suspensions of tiny particles. *Phys. Rev. Fluids* **2** (3), 034304.

GUALTIERI, P., PICANO, F. & CASCIOLA, C. M. 2009 Anisotropic clustering of inertial particles in homogeneous shear flow. *J. Fluid Mech.* **629**, 25–39.

GUNN, D. J. 1978 Transfer of heat and mass to particles in fixed and fluidised beds. *Intl J. Heat Mass Transfer* **21**, 467–476.

HENDERSON, B. 2010 Fifty years of fluidic injection for jet noise reduction. *Intl J. Aeroacoust.* **9** (1-2), 91–122.

HIMELBLAU, H., KERN, D. L., MANNING, J. E., PIERSOL, A. G. & RUBIN, S. 2001 Dynamic environmental criteria. *NASA Tech. Handbook* NASA-HDBK-7005.

HOUIM, R. W. & ORAN, E. S. 2016 A multiphase model for compressible granular–gaseous flows: formulation and initial tests. *J. Fluid Mech.* **789**, 166–220.

IGNATIUS, J. K., SATHIYAVAGEESWARAN, S. & CHAKRAVARTHY, S. R. 2014 Hot-flow simulation of aeroacoustics and suppression by water injection during rocket liftoff. *AIAA J.* **53** (1), 235–245.

JORDAN, P. & COLONIUS, T. 2013 Wave packets and turbulent jet noise. *Annu. Rev. Fluid Mech.* **45** (1), 173–195.

KALTENBACH, M., MASCHKE, C. & KLINKE, R. 2008 Health consequences of aircraft noise. *Dtsch. Arztebl Int.* **105** (31–32), 548–556.

KLEINMAN, R. & FREUND, J. B. 2008 The sound from mixing layers simulated with different ranges of turbulence scales. *Phys. Fluids* **20** (10), 101503.

KROTHAPALLI, A., VENKATAKRISHNAN, L., LOURENCO, L., GRESKA, B. & ELAVARASAN, R. 2003 Turbulence and noise suppression of a high-speed jet by water injection. *J. Fluid Mech.* **491**, 131–159.

LAUFER, J. 1961 Aerodynamic noise in supersonic wind tunnels. *J. Aero. Sci.* **28** (9), 685–692.

LAUFER, J., SCHLINKER, R. & KAPLAN, R. E. 1976 Experiments on supersonic jet noise. *AIAA J.* **14** (4), 489–497.

LEBOISSETIER, A., OKONG'O, N. & BELLAN, J. 2005 Consistent large-eddy simulation of a temporal mixing layer laden with evaporating drops. Part 2. *A posteriori* modelling. *J. Fluid Mech.* **523**, 37–78.

LHUILLIER, D., THEOFANOUS, T. G. & LIOU, M. 2010 Multiphase flows: compressible multi-hydrodynamics. In *Handbook of Nuclear Engineering*, pp. 1813–1912. Springer.

LIGHTHILL, M. J. 1952 On sound generated aerodynamically I. General theory. *Proc. R. Soc. Lond.* A **211** (1107), 564–587.

LIGHTHILL, M. J. 1956 Viscosity effects in sound waves of finite amplitude. In *Surveys in Mechanics* (ed. G. K. Batchelor & R. M. Davies), pp. 250–351. Cambridge University Press.

LING, Y., BALACHANDAR, S. & PARMAR, M. 2016 Inter-phase heat transfer and energy coupling in turbulent dispersed multiphase flows. *Phys. Fluids* **28** (3), 033304.

MARCHIOLI, C. & SOLDATI, A. 2002 Mechanisms for particle transfer and segregation in a turbulent boundary layer. *J. Fluid Mech.* **468**, 283–315.

MATTSSON, K., SVÄRD, M. & NORDSTRÖM, J. 2004 Stable and accurate artificial dissipation. *J. Sci. Comput.* **21** (1), 57–79.

MEHRABADI, M., TENNETI, S., GARG, R. & SUBRAMANIAM, S. 2015 Pseudo-turbulent gas-phase velocity fluctuations in homogeneous gas–solid flow: fixed particle assemblies and freely evolving suspensions. *J. Fluid Mech.* **770**, 210–246.

MILLER, R. S. & BELLAN, J. 1999 Direct numerical simulation of a confined three-dimensional gas mixing layer with one evaporating hydrocarbon-droplet-laden stream. *J. Fluid Mech.* **384**, 293–338.

MURRAY, N. E. & LYONS, G. W. 2016 On the convection velocity of source events related to supersonic jet crackle. *J. Fluid Mech.* **793**, 477–503.

NICOLAI, C., JACOB, B. & PIVA, R. 2013 On the spatial distribution of small heavy particles in homogeneous shear turbulence. *Phys. Fluids* **25** (8), 083301.

NORUM, T. D. 2004 Reductions in multi-component jet noise by water injection. In *10th AIAA/CEAS Aeroacoustics Conference, AIAA Paper* 2004-2976.

NOYMER, P. D. & GLICKSMAN, L. R. 2000 Descent velocities of particle clusters at the wall of a circulating fluidized bed. *Chem. Engng Sci.* **55** (22), 5283–5289.

OKONG'O, N. A. & BELLAN, J. 2004 Consistent large-eddy simulation of a temporal mixing layer laden with evaporating drops. Part 1. Direct numerical simulation, formulation and *a priori* analysis. *J. Fluid Mech.* **499**, 1–47.

PANTANO, C. & SARKAR, S. 2002 A study of compressibility effects in the high-speed turbulent shear layer using direct simulation. *J. Fluid Mech.* **451**, 329–371.

PAPAMOSCHOU, D. 2000 Linear model of Mach wave suppression in a dual-stream jet. In *6th Aeroacoustics Conference and Exhibit*. AIAA.

PARMAR, M., HASELBACHER, A. & BALACHANDAR, S. 2012 Equation of motion for a sphere in non-uniform compressible flows. *J. Fluid Mech.* **699**, 352–375.

PHILLIPS, O. M. 1960 On the generation of sound by supersonic turbulent shear layers. *J. Fluid Mech.* **9**, 1–28.

REEKS, M. W. 1983 The transport of discrete particles in inhomogeneous turbulence. *J. Aero. Sci.* **14** (6), 729–739.

RIBNER, H. S. 1962 Aerodynamic sound from fluid dilatations. *Tech. Rep.* 86. University of Toronto Inst. Aerophysics.

RISTORCELLI, J. R. 1997 Fluctuating dilatation rate as an acoustic source. *Tech. Rep.* Institute for Computer Applications in Science and Engineering.

ROUSON, D. W. I. & EATON, J. K. 2001 On the preferential concentration of solid particles in turbulent channel flow. *J. Fluid Mech.* **428**, 149–169.

SARKAR, S. 1992 The pressure–dilatation correlation in compressible flows. *Phys. Fluids* **4** (12), 2674–2682.

SCHILLER, L. & NAUMANN, A. 1933 Fundamental calculations in gravitational processing. *Z. Verein. Deutsch. Ing.* **77**, 318–320.

SHAFFER, F., GOPALAN, B., BREAULT, R. W., COCCO, R., KARRI, S. B., HAYS, R. & KNOWLTON, T. 2013 High speed imaging of particle flow fields in CFB risers. *Powder Technol.* **242**, 86–99.

STRAND, B. 1994 Summation by parts for finite difference approximations for d/dx. *J. Comput. Phys.* **110** (1), 47–67.

SVÄRD, M., CARPENTER, M. H. & NORDSTRÖM, J. 2007 A stable high-order finite difference scheme for the compressible Navier–Stokes equations, far-field boundary conditions. *J. Comput. Phys.* **225** (1), 1020–1038.

TENNETI, S., GARG, R. & SUBRAMANIAM, S. 2011 Drag law for monodisperse gas-solid systems using particle-resolved direct numerical simulation of flow past fixed assemblies of spheres. *Intl J. Multiphase Flow* **37** (9), 1072–1092.

TENNETI, S., SUN, B., GARG, R. & SUBRAMANIAM, S. 2013 Role of fluid heating in dense gas–solid flow as revealed by particle-resolved direct numerical simulation. *Intl J. Heat Mass Transfer* **58** (1), 471–479.

VISHNAMPET, R. 2015 An exact and consistent adjoint method for high-fidelity discretization of the compressible flow equations. PhD thesis, University of Illinois at Urbana-Champaign.

VISHNAMPET, R., BODONY, D. J. & FREUND, J. B. 2015 A practical discrete-adjoint method for high-fidelity compressible turbulence simulations. *J. Comput. Phys.* **285**, 173–192.

VREMAN, A. W., SANDHAM, N. D. & LUO, K. H. 1996 Compressible mixing layer growth rate and turbulence characteristics. *J. Fluid Mech.* **320**, 235–258.

ZOPPELLARI, E. & JUVE, D. 1997 Reduction of jet noise by water injection. In *3rd AIAA/CEAS Aeroacoustics Conference*, *AIAA Paper* 97-1622, pp. 267–274.